Characterization of the solids crossflow in a bubbling fluidized bed

Powder Technology 443 (2024) 119967

Contents lists available at ScienceDirect

Powder Technology

journal homepage: www.journals.elsevier.com/powder-technology

Characterization of the solids crossflow in a bubbling fluidized bed

Munavara Farha *, Diana Carolina Guío-Pérez, Filip Johnsson, David Pallarès

Chalmers University of Technology, Hörsalsvägen 7B, 412 96 Gothenburg, Sweden

HIGHLIGHTS

- Horizontal solids transport in BFBs with crossflow is characterized through magnetic tracer measurements.
- Convective/dispersive transport, RTDs, flow behavior, and overall fluidization quality assessed.
- Three analytical methods examined: deconvolution, convection-dispersion, and compartment modeling.
- Data fit to convection-dispersion model shows linear relation between dispersion coefficient and velocity.
- Data fit to compartment model shows reduced dead zone with higher solids crossflow, bed height, and velocity.

GRAPHICAL ABSTRACT

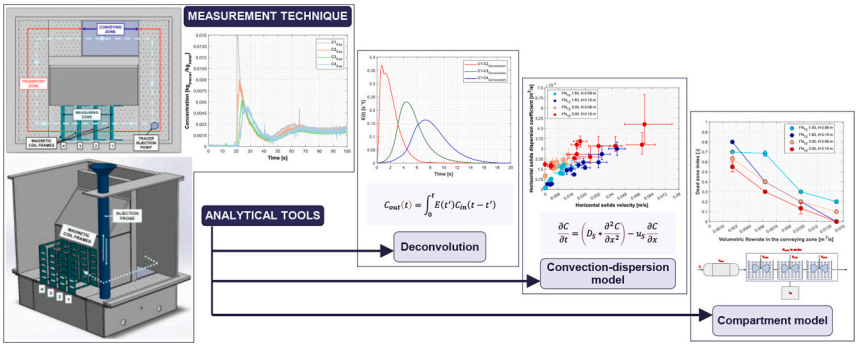

ARTICLE INFO

Keywords:
Bubbling fluidized bed
Solids mixing
Compartment modeling
Solids convection
Solids dispersion
Solids residence time distribution

ABSTRACT

The horizontal transport of solids in bubbling fluidized beds that have a solids crossflow is characterized by applying magnetic tracer measurements and modeling techniques to determine: the contributions of convective and dispersive forms of transport of solids; the residence time distributions of the solids; the feasibility of achieving a plug-flow or well-stirred tank behavior of the solids flow; and the overall fluidization quality. The latter is quantified by determining the extent of de-fluidized zones under varying operational conditions.

The experiments are conducted in a bubbling fluidized bed with different rates of forced horizontal flow of solids, applying different bed heights and fluidization velocities. The setup is designed and operated in accordance with Glicksman's full set of scaling laws for fluidized beds, allowing scaling-up of the results to hot, large-scale conditions that resembling, for example, indirect gasification. The assessment of horizontal solids flow involves the sampling of a ferromagnetic tracer using impedance measurements at distinct locations within the bed to: i) fit the convection-dispersion transport equation and, thereby, determine the horizontal dispersion coefficient and velocity of the solids; and ii) feed a deconvolution routine for studying reduced-order (simplified) representations of the solids flow through compartment models.

The results from the fitting to the convection-dispersion equation show a strong and close-to-linear correlation between the horizontal solids dispersion coefficient and the forced horizontal solids velocity. This strong interdependency may be attributable to increased shear-related mixing at higher bed-wall shear rates, and it implies a greater challenge linked to attaining a convection-controlled (plug flow) pattern for the solids crossflow. The residence time distributions obtained reveal the limitations of the convection-dispersion equation in providing a general description of the solids flow. Compartment model fitting, when applied to the observed

* Corresponding author.
E-mail address: m.farha@chalmers.se (M. Farha).

https://doi.org/10.1016/j.powtec.2024.119967
Received 23 December 2023; Received in revised form 12 May 2024; Accepted 3 June 2024
Available online 4 June 2024

residence time distributions, reveals that an increase in solids crossflow or, to a lesser extent, increased bed height leads to improved fluidization quality.

1. Introduction

The fluidized bed technology for industrial applications has witnessed a surge in relevance in the last few decades. This applies particularly to the energy sector, due to the strong demand for fuel-flexible units that provide efficient thermochemical conversion of solid feedstocks with various properties (from the original use of coal to the later introduction of biomass and waste) and blends thereof [1,2]. The performance of a fluidized bed unit is governed by a complex interplay between fluid mechanics, kinetics, and heat transfer, which yields comparatively faster rates of mixing and mass and heat transfer [3,4]. Despite this fundamental complexity, development of the technology, much of which has been achieved through empirical experience, has yielded mature designs for fluidized bed reactors over a broad spectrum of industrial sectors, e.g., petrochemical, pharmaceutical, chemical, food, mining, and energy conversion [1,2]. In the energy sector, the fluidized bed technology has proven efficient for processes of pyrolysis, gasification, and combustion [1]. While the technological development of such reactors has been successful, the experience-based nature of the reactor development limits further development, including new applications. This is evident from the slow development pace and the high incidence of troubleshooting during operation. Thus, development of fluidized bed technology is increasingly dominated by the combined use of modeling tools and dedicated measurements that target the core understanding of specific phenomena.

Furthermore, the fluidized bed technology exists in the forms of stationary bubbling fluidized beds [BFBs] and circulating fluidized beds, allowing for more-complex reactor types and systems [5]. These include reactors with a significant solids throughput, which are found as standalone reactors or reactors that are interconnected with another fluidized bed unit within a dual fluidized bed (DFB) system. These reactors are intended for use in systems that apply solids circulation, such as in gasification and various reduction- oxidation (redox) cycles.

The standalone BFB system with solids crossflow is widely used in applications such as drying, iron ore reduction, pharmaceuticals, and waste incineration. In the case of pharmaceuticals, BFB systems ensure controlled particle size in granulation processes, so as to ensure consistent product quality [6]. For drying, the BFB's uniform heat and mass transfer capabilities enable precise control of the product's moisture content [3]. In iron ore reduction, the efficient heat and mass transfer of BFBs accelerates the reaction kinetics [2,4]. In waste incineration, the BFB's versatility in handling diverse waste types, coupled with solids crossflow, enhances combustion efficiency [3].

The DFB systems are applied in various industrial processes, particularly those in which strategic management of solid particles and precise control of reactor conditions are crucial. The characteristic fluid-like behavior of fluidized beds makes them a favorable choice for applications that require the transfer of solids between reactors, particularly when transfer occurs in distinct atmospheres or under specific reaction conditions. This feature is crucial for the fluid catalytic cracking (FCC) units in petroleum refining processes, wherein the DFB system facilitates the circulation of catalyst particles between the cracking reactor and a regenerator, each of which operates under different conditions [1–4]. Thus, DFB systems can provide independent control and optimization of the operation of each reactor in a DFB loop. For example, in indirect gasification processes, the integration of a combustor is crucial for preheating the gasification agent, enhancing the quality of the produced syngas and the overall efficiency of biomass conversion. Separate optimization of the gasifier and combustor steps is vital for this process [1,4]. Similarly, in chemical looping combustion (CLC) for CO_2 capture, DFBs facilitate constant and controllable solids transfer, while preventing air-in leakage to the fuel reactor [7]. Thus, the process has the potential to achieve high efficiency.

BFBs and DFBs have a wide range of potential applications in the energy transition involving solids crossflows. Therefore, comprehending the intricate dynamics that govern the solids crossflow is essential. This includes understanding the mechanisms and patterns that influence the crossflow behavior in a BFB, as these are critical for optimizing the performance in various applications. Given the complexity of bubble phenomena in a BFB, which involves convective bubble flow and fine-grained processes, it is crucial to understand how dispersive and convective dynamics influence the flow of solids across the bed. Although the existing literature primarily treats horizontal solids transport as a dispersion-type phenomenon, a notable gap in the knowledge exists in relation to the motion of macroscopic solids.

Several studies have explored the crossflow of solids and its subsequent impact on the gas-solids mixing in fluidized bed systems. Kong et al. [8] analyzed a laboratory-scale, crossflow BFB with Geldart group A-powders, using tracer stimulus-response for the residence time distribution (RTD) measurement. They showed that baffles placed in the reactor enhance plug flow and significantly improve gas-solids mixing, both of which are beneficial for drying and thermal processing. Geng et al. [9] investigated the RTD of solids in crossflow BFBs, employing CFD simulations corroborated by experiments in a laboratory-scale DFB setup with silica sand and coal particles (tracers). The key findings were that bed height and solids flux significantly influence the RTD of solids, which is crucial for optimizing chemical and heat looping processes. Specifically, an increased bed height extended the solids' residence time, while variations in the solids flux sharply increased the peaks of the RTD curves.

Sette et al. [10] investigated the impact of bulk solids crossflow on fuel particle mixing in DFB systems, targeting applications such as CLC and indirect biomass gasification. Utilizing a downscaled cold flow model with aluminum and polyamide particles (tracers), they showed that the bulk solids crossflow significantly influences the velocity field and mixing of fuel particles. Their analysis, integrating potential flow theory and diffusion equations, demonstrated that convective transport is vital for accurately deriving the fuel particle dynamics, and that it differs significantly from the average lateral velocity of bulk solids. Guío-Pérez et al. [11] analyzed the RTD in a secondary reactor of a dual circulating fluidized bed (DCFB) for chemical looping, using a cold flow model and inductance-based measurement with steel particles as tracers. Their study revealed that the global circulation rate inversely influences the mean residence time across both global and internal loops, while the reactor fluidization velocity specifically affects the RTD of the internal loop. A modular model that integrates ideal plug flow and stirred tank reactors was employed, to capture accurately the flow patterns and bed density variations within the reactor.

Vollmari et al. [12] conducted an RTD study in dual-chamber fluidized beds, focusing on the effects of operational parameters such as mass inflow, fluidization velocity, and particle characteristics. Utilizing radio frequency identification (RFID) technology and DEM-CFD simulations, they revealed that changes in operational parameters significantly affect the solids crossflow and mixing, with consequent impact on the RTD. Moreover, that study emphasized the importance of solids interchange between chambers for efficient and uniform mixing, which is crucial for granulation and coating applications. Hua et al. [13] explored the (solids) RTD in a gas-solid dense fluidized bed with baffles, using a two-phase Eulerian-Eulerian model alongside the kinetic theory of granular flow. Their analysis was validated by a 3D laboratory-scale, cold-flow model with non-spherical particles, which measured the solids hydrodynamics by sampling bed material at the outflow. The results

showed that baffles significantly enhance the plug flow and reduce lateral dispersion. A combination of 1D plug flow, dispersion model, and tanks-in-series model was applied for the RTD analysis.

Schlichthaerle and Werther [14] investigated solid mixing dynamics within a cold model CFB riser, utilizing solid carbon dioxide as tracer. They demonstrated that the convective flow of externally circulated solids significantly enhances horizontal mixing in the CFB's bottom zone, leading to more-uniform temperature and solids distribution, as confirmed by a transient 1D convection-dispersion model. Gan et al. [15] examined particle mixing in a quasi-slot-rectangular spouted bed model, employing a 1D convection-dispersion model for the analysis. They observed that: a higher superficial gas velocity intensifies bubble activity for greater dispersion, increases the static bed height, and enhances bubble dynamics for more-effective tracer mixing; and a wider air inlet section improves bubble flow while reducing wall effects, altogether contributing to more-efficient lateral particle dispersion and distribution uniformity across the bed.

The reviewed literature effectively illustrates an understanding of dispersion and convection effects in crossflow beds. However, it also highlights a significant knowledge gap in terms of identifying the optimal operational parameters for improving system efficiency. Given the intricate nature of particle behaviors under different conditions in fluidized beds with a crossflow of solids, there is a need for a more-comprehensive understanding of the dynamics of the gas-solids flows in such beds. It is of particular interest to measure the solids mixing, so as to identify strategies to control the RTD, which is a key factor in the overall performance of fluidized beds with a crossflow of solids. Therefore, it is important to investigate quantitatively the interplay between the convection and dispersion of solids, as well as to address the non-ideal features of solids transport mechanisms.

In addressing the gaps identified above, this study aims to characterize the solids mixing established in BFBs with horizontal solids crossflows. More specifically, this work seeks to: i) elucidate the impacts of operational parameters, i.e., bed height, fluidization velocity, and solids crossflow rate, on the resulting horizontal solids transport; ii) assess the validity of the convection-dispersion transport equation as a way of describing the solids flow established; and iii) evaluate the extent of de-fluidized ("dead") zones. This work combines magnetic solids tracing measurements, analysis of the solids RTDs derived from experimental data deconvolution, and modeling (including a transient 1D convection-dispersion framework and a compartment model). The experiments described in this study were conducted in a fluid-dynamically scaled-down unit bubbling bed that was operated under ambient conditions with Geldart group B solids.

2. Theory

In the present work, well-established methods are used to define the characteristics of the flow inside a specific volume within a fluidized bed. Given a known geometry and the availability of tracer concentration profiles at different positions and resolved in time, the analysis entails the extraction and description of RTD curves, and assessments of two different flow models: one that is based on a convection-dispersion equation; and one that is based on the combination of ideal compartments.

2.1. Residence time distribution

A common practice in the design and study of reactors is to analyze the RTD, which can be derived from regular tracer experiments through the deconvolution of the experimentally acquired tracer input, $C_{in}(t)$, and response, $C_{out}(t)$, functions [16,17]. The shape of the RTD curve provides quantitative insights into specific flow characteristics, such as the bypass flow through the bed, recirculation of solids, and stagnant zones in the bed. The analytical relationship between the tracer input function and the response function can be written as:

$$C_{out}(t) = \int_0^t E(t')C_{in}(t-t') \tag{1}$$

Statistical metrics are used to characterize the RTD curves [16,17]. The first moment, 'mean residence time', signifies the average time that a particle spends within the system before it exits the measurement volume of the bed, as in Eq. (2). The second moment, 'variance', quantifies the spread or dispersion of the residence times around the mean, as expressed by Eq. (3):

$$\tau = \int tE(t)dt \tag{2}$$

$$\sigma^2 = \int (t-\tau)^2 E(t)dt \tag{3}$$

2.2. Convection-dispersion model

The horizontal transport of solids in a BFB can be assumed to be a combination of dispersion- and convection-like movements of the solids with an imposed crossflow of solids [3,18]. This solids mixing is generally linked to the gas-solids flow structures that arise from the bubble flow [3,18]. In BFBs, vertical solids mixing generally occurs at a rate that is an order of magnitude higher than horizontal mixing [19–21]. Combined with the low bed heights relative to the cross-sectional dimensions, this results in rapid tracer homogenization in the vertical direction. Consequently, the vertical dimension can be considered as being perfectly mixed and is disregarded in the study of the solids mixing. Similarly, given that the length of the channel is much shorter than its width, solids mixing perpendicular to the net solids throughput is disregarded in this study of the movement of solids along the horizontal flow direction in a channel. Therefore, a transient, 1-dimensional, convection-dispersion model can be employed to derive a macroscopic description of the horizontal transport of solids in BFBs with horizontal solids crossflow [22]:

$$\frac{\partial C}{\partial t} = \left(D_S{}^*\frac{\partial^2 C}{\partial x^2}\right) - u_S\frac{\partial C}{\partial x} \tag{4}$$

Thus, in the case of a forced horizontal crossflow of solids, the solids convection corresponds to the horizontal macroscopic movement of the particles, driven by the forced crossflow of solids [3,18]. The horizontal dispersion of solids is assumed to correspond to a random-type mixing of particles [3,18].

Furthermore, the relative contributions of convective transport and dispersive mixing can be quantified using a dimensionless parameter, the Péclet (Pe) number, as demonstrated in Eq. (5):

$$Pe = \frac{u_S \cdot L}{D_S} \tag{5}$$

A high Pe number indicates a mixing pattern that more closely resembles a plug flow, whereas low Pe values indicate a flow that is well-mixed.

2.3. Compartment model

Analytical expressions that describe singular flow patterns can be found in the reactor design literature. Although real systems obviously differ from an ideal system, they can still be represented by a combination of analytical expressions. A compartment model [16,17] can be used to represent the mixing within a reactor using a combination of interconnected subunits (also called *compartments*), as shown in Fig. 1, with each compartment embodying a unique hydrodynamic behavior (perfectly mixed, plug flow, stagnant). Through the selection of an appropriate compartment configuration, this type of model can accurately represent flow behaviors. This strategy facilitates the quantification of phenomena such as dead zones through the fitting of

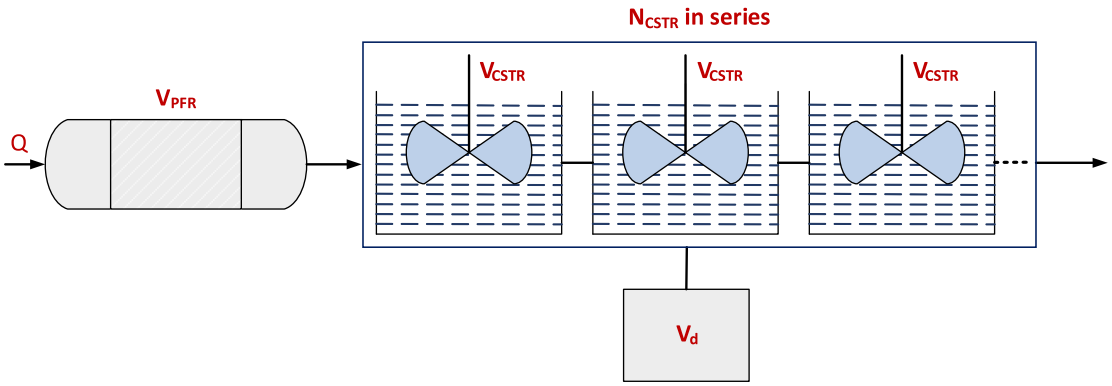

Fig. 1. Schematic representation of the compartment model used in this work, encompassing a PFR, a CSTR series, and a stagnant compartment.

experimental RTD data to specific parameters of the compartment model.

The compartment model used in this study (Fig. 1) encompasses a primary stream of solids with volumetric flowrate Q. The mixing of solids along the solids flow direction is represented by a series of continuously stirred tank reactors (CSTRs), while the purely convective part of the flow (due to the forced circulation of solids) is represented by a plug flow reactor (PFR). The former part is defined by two parameters: the number of CSTRs, N_{CSTR}; and the volume of each CSTR, V_{CSTR}. The latter is defined by a single parameter: the volume of the PFR, V_{PFR}. The number of reactors directly impacts the extent of mixing within the system. A component that exhibits stagnant flow is added to represent the possible presence of de-fluidized regions, also known as *dead zones* with volume V_d, which effectively reduce the active volume available for solids flow in practice.

Eq. (6) presents the analytical expression for the flow through the system illustrated in Fig. 1. More specifically, the equation indicates how the analytical equation (and the variables used to characterize the compartment system) can be used to calculate the transient outlet concentrations of tracer solids (also called the *response function*) based on a given input function. In this equation, M is the mass of tracer solids injected.

$$C_{out}(t) = C_{in}(t) + \frac{M}{Q}\left\{\frac{1}{\tau(1-i_d)}\frac{{N_{CSTR}}^{N_{CSTR}}}{(N_{CSTR}-1)!}\left[\frac{(t-\tau_{PFR})}{\tau(1-i_d)}\right]^{N_{CSTR}-1}\right\} e^{-N_{CSTR}\frac{(t-\tau_{PFR})}{\tau(1-i_d)}} \tag{6}$$

Here, τ denotes the mean residence time of the tracer solids, and i_d represents the ratio of the dead zone volume V_d to the total system volume.

3. Experimental work

This section outlines the design and fluid-dynamical scaling of the cold flow model used in this work, describes the application of the magnetic solids tracing technique to monitor the transient concentration profile of tracer solids that are injected into the bed of the cold flow model, the process used for measurement data validation through signal calibration and quality assessment, and the experimental matrix, specifying the value ranges of the operational parameters.

3.1. Experimental setup

The fluid-dynamically down-scaled cold model resembles the fluidization of sand (mean size, 125 μm) with air or flue gas at 800 °C (corresponding to the conditions used in typical energy conversion applications, e.g., combustion, gasification, and pyrolysis). The cold flow model features a rectangular cross-section of 0.5 m × 0.4 m, with a length scaling factor of 0.12 with respect to up-scale hot conditions (based on Glicksman's simplified set of scaling laws [23,24]). The cold flow model features a solids horizontal circulation loop in which a horizontal flow of solids is conveyed in a clockwise direction. This type of configuration is commonly applied in applications such as CLC, biomass gasification, integrated gasification combined cycle, fluid catalytic cracking in petroleum refining, etc. [3,4,18]

A channel is formed by placing a block in the center of the unit through which the solids circulate (Fig. 2). The channel is fluidized with a similar velocity at all points, except for the conveying zone. Within the conveying zone, a different flow regime is implemented, one that is characterized by a fluidization velocity that is higher than that of the transport zone. This modification is crucial for enabling the horizontal conveyance of solids, distinguishing it from the bubbling conditions prevalent in the transport zone. For the control of solids circulation, a conveying mechanism based on a combination of high-velocity nozzles and baffles (here called the *conveying zone*) is integrated into the loop. The specific design and mechanisms of this section are not disclosed due to a confidentiality agreement and are, thus, outside the scope of this work. The fluidized solids flow is transported through a so-called *transport region* to the measuring zone where it is investigated using magnetic tracing (see **Section 3.2**). For this purpose, four coils are installed in the measuring zone. The circulation loop is completed by an additional fluidized transport zone that connects with the conveying section.

As indicated above, the simplified set of fluid-dynamical scaling laws (referenced as [24]) has been applied to design the experimental unit with an appropriate length scaling factor. This factor has been chosen as 0.12, primarily to align with the constraints related to the laboratory infrastructure and the available bed materials. Table 1 presents a comparison of the cold flow model and its hot scale unit counterpart in terms of the operational conditions and bed materials used.

3.2. Measurement technique

A solids tracing technique is used in the present work to evaluate the flow pattern of the solids stream in the measuring zone (indicated in **Section 3.1**). The magnetic solids tracing technique [11,25,26] selected for this purpose operates on the principle that materials with distinct magnetic permeabilities induce different impedance values within a designated coil, thereby enabling the quantification of the concentration of a magnetic material through measurement of the impedance of the coil. In this study, the coils are designed to span the entire solids flow cross-section of the channel. This configuration produces a one-dimensional concentration profile along the solids flow direction that reflects the tracer intensity, as the solids are transported horizontally, and it is not affected by variations in concentration across the channel's height or width [26].

In order to be implemented for quantitatively assessing the flow dynamics of bulk solids in fluidized beds, the magnetic tracer particles

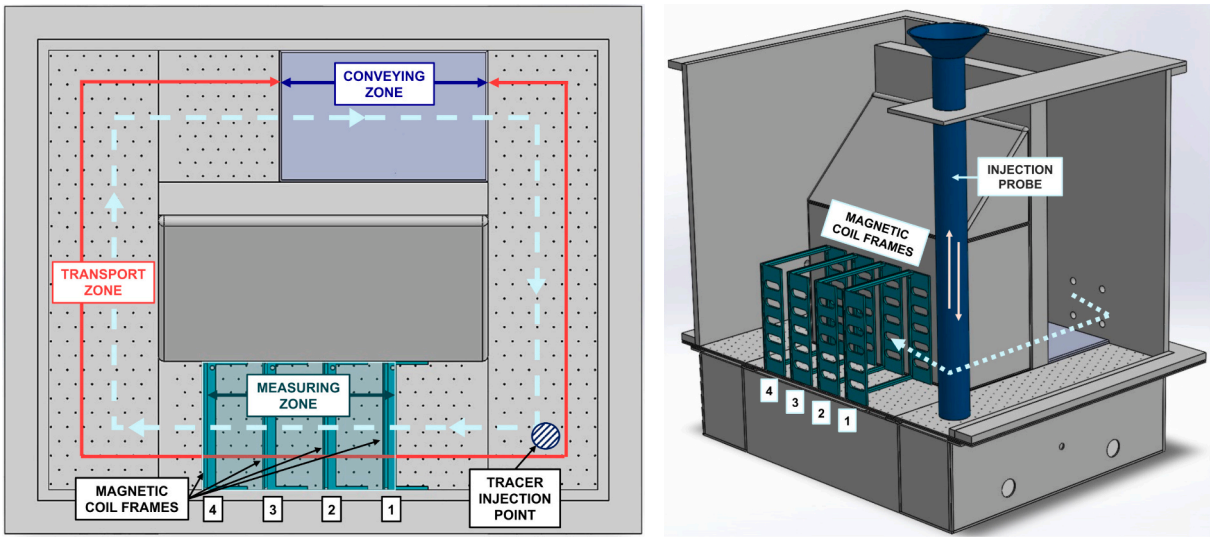

(a) Top view (b) Isometric view

Fig. 2. Fluid-dynamically down-scaled model used in the experiments, where the clockwise circulation of solids is forced in the conveying section and diagnosed by coil measurements in the measuring zone.

Table 1
Main parameters used in the fluid-dynamic scaling.

Parameter	Units	Hot unit	Cold model
Temperature	°C	800	24
Fluidization gas		Hot air or flue gases	Air
Gas density (ρ_F)	kg/m^3	0.359	1.187
Gas viscosity (μ_F)	m^2/s	1.4×10^{-4}	1.54×10^{-5}
Bed geometry	m	L_{HOT}	$0.12 L_{HOT}$
Bed material		Silica sand	Bronze
Particle density (ρ_S)	kg/m^3	2650	8770
Mean particle diameter (d_S)	μm	950	125
Gas superficial velocity (u_0)	m/s	$u_{0,\mathrm{HOT}}$	$\sqrt{0.12}\, u_{0,HOT}$
Minimum fluidization velocity (u_{mf})	m/s	0.31	0.108
Horizontal solids mean velocity (u_S)	m/s	$u_{S,HOT}$	$0.347 \cdot u_{S,HOT}$
Horizontal solids dispersion coefficient (D_S)	m^2/s	$D_{S\,HOT}$	$0.042 \cdot D_{S\,HOT}$

must mirror the flow pattern of the bed material to the greatest extent possible. This can be achieved by choosing a tracer material that has physical properties similar to those of the bed material. This work applies an Fe-based tracer material (with a magnetic susceptibility of 0.9) to mimic the flow dynamics of the bronze (with a magnetic susceptibility of 0) used as the bed material. Table 2 lists the physical properties of both materials, together with the *Ar*-based dimensionless particle sizes.

The measurement zone, which has a cross-sectional area of 0.16 × 0.12 m, is equipped with four coils (see Fig. 2). The magnetic field created by these coils effectively covers the specified cross-sectional area. The coils are located at a distance of 0.055 m from each other. For each experiment, a batch of 200 g of tracer particles (representing 0.25%–0.32% of the total solids inventory) is introduced into the fluidized bed 14 cm upstream of Coil 1 (see Fig. 2a), using a special injection probe, which allows premixing of the tracer with the bed material in the vertical direction before injection. In this way, the tracer captures the flow pattern of the solids flow throughout its entire depth. With this setup, the transient tracer concentration profiles can be sampled (at a frequency of 100 Hz) by the four coils, i.e., at four different locations along the measurement zone shown in Fig. 2.

3.3. Quantification of experimental uncertainty

Quantification the uncertainty of the experimental data is essential to assess the reliability of the results obtained from the analysis [27]. This section describes the measures taken to validate the integrity of the

Table 2
Comparison of the bed material and magnetic tracer.

Parameter	Unit	Bed material	Tracer
Material	–	Bronze	Iron-based alloy
Particle density (ρ_S)	kg/m^3	8770	7988
Bulk density (ρ_B)	kg/m^3	5522	4520
Particle size distribution d_{10}-d_{50}.d_{90}	μm	80–112–132	25–69–123
Sauter mean diameter (d_{32})	μm	126.137	102.472
$Ar^{1/3}$	–	8.386	6.127
Minimum fluidization velocity (u_{mf})	m/s	0.074	0.039
Magnetic susceptibility	–	0	0.9

measured data, with particular emphasis on signal calibration and signal quality assessment.

A signal of impedance, Z, against time is acquired from each coil and thereafter converted into tracer concentration values according to Eq. (7):

$$C = k \cdot \frac{(Z - Z_0)}{Z_0} \tag{7}$$

where Z_0 is the natural impedance of the coil and k is an inductance calibration coefficient. This coefficient depends on the tracer material (through its relative permeability) and the ability of the coil to capture the presence of a tracer material when it is distributed within the volume occupied by the magnetic field of the coil. The values of k are in the range of 0.8–1.6 $\frac{kg_{tracer}}{kg_{total}}$, with a calibration uncertainty range within the range of 0.03–0.3% (see **Appendix A**).

The Signal-to-Noise ratio [SNR, see Eq. (8)] was calculated to assess the signal quality. The SNR represents the ratio of the amplitude of the peak signal to that of the inherent background noise. The determination of signal uncertainty is based upon the standard deviation of SNR values calculated across diverse data segments [28]. This approach assumes the stationarity of the statistical attributes of both the signal and noise. In the equation given below, A_{signal} represents the amplitude of the primary concentration signal being measured and A_{noise} denotes the amplitude of the noise, encompassing all unwanted or interfering signals that disrupt the clarity of the primary signal. Note that a fixed window size of 100 samples is chosen to calculate the SNR, whereby for each window, the noise is determined by subtracting the mean of the signal segment from each data-point within that window.

$$\text{SNR (dB)} = 20log_{10}\left(\frac{A_{signal}}{A_{noise}}\right) \tag{8}$$

Fig. 3 illustrates the characterization of the SNR values for the concentration measurements performed in the present study. Fig. 3a shows an example of typical transient profiles of the raw concentration signals measured by each of the four coils (C1 to C4) during a tracer experiment. Fig. 3b presents the corresponding SNR profiles calculated using Eq. (8). Finally, Fig. 3c summarizes the assessment of SNR over the full range of

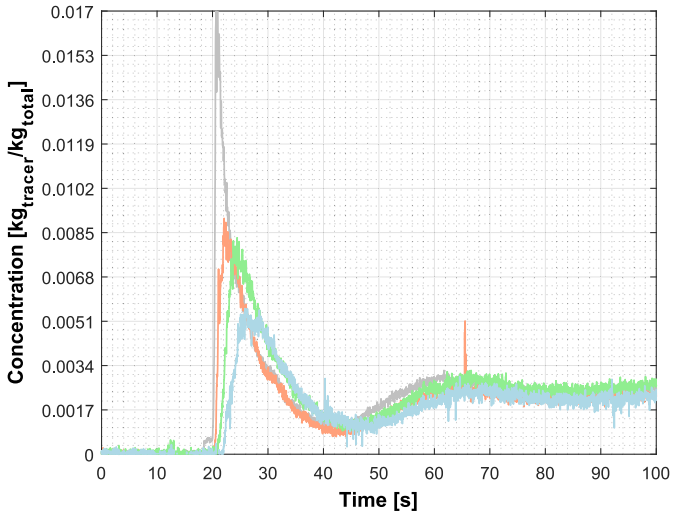

(a) Transient profile of the measured tracer concentration (FN_{TZ}=3, H=0.08 m, Q_{CZ}=0.0143 m^3/s)

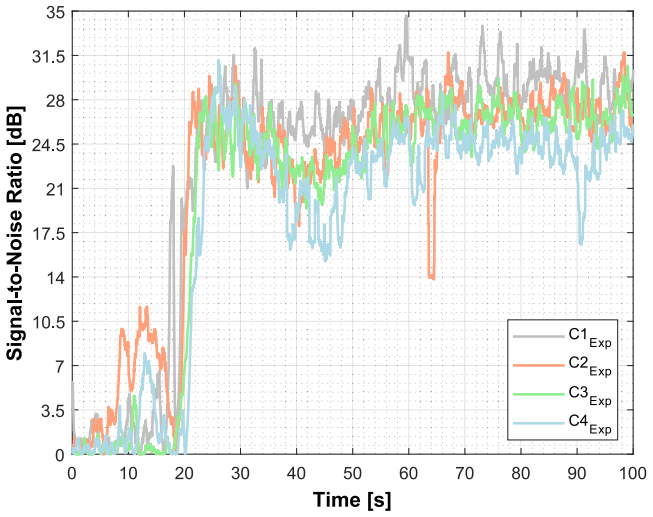

(b) Transient profile of the signal-to-noise ratio (under same conditions as in Figure 3a)

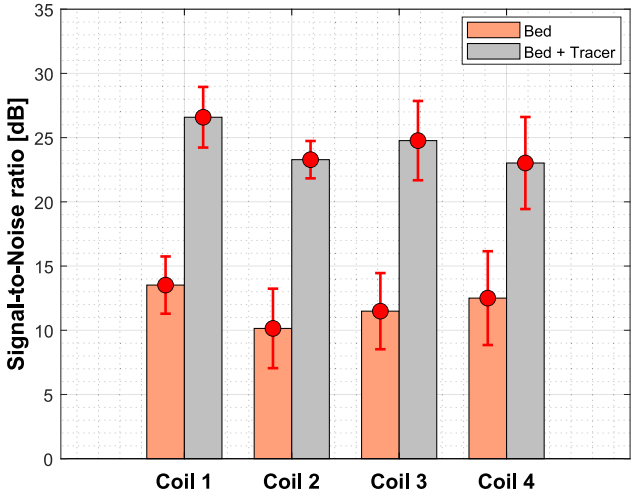

(c) Variability of the signal-to-noise ratio across diverse operational conditions with and without tracer material.

Fig. 3. Characterization of the signal-to-noise ratio.

operational conditions applied in this work (see Section 3.4), as well as with and without tracer. In the absence of a tracer, the measurements yield a constant flat-line concentration signal. In Fig. 3c, these conditions are depicted as gray and orange bars, respectively. The analysis highlights distinct trends in the signal strength and noise levels. Notably, across all four coils, there is a consistent range of the SNR of 23–27 dB when tracer material is present, and of 7–17 dB in the absence of a tracer. For a specific coil, the variability obtained across all operational conditions applied, as indicated by the red bars in Fig. 3c, is relatively minor. This suggests that the operational conditions have limited impacts on the SNR, indicating that the coils maintain a stable relationship between the desired signal strength and background noise across operational variations. Overall, it is concluded that the method can provide reliable concentration measurements in fluidized beds under the conditions applied in this work.

The adoption of low-pass filters [29] has emerged as a suitable approach to mitigating the undesired, high-frequency noise components inherent to the acquired signals, while maintaining the lower frequencies corresponding to the gas-solids flow of the process. Thus, a specific low-pass filter with a cutoff frequency of 7.5 Hz is selected. This selection is grounded in a referenced methodology, wherein the cutoff frequency is determined as that at which the cumulative sum of the power spectral density reaches 95% of the total signal power [30].

3.4. Test matrix

In the present investigation, the experimental matrix comprises three variable operational parameters: fluidization number in the bed, FN_{TZ} (u_0/u_{mf}) = 1.83–3; static bed height, H = 0.08–0.10 m; and volumetric air flowrate injected in the conveying zone, Q_{CZ} = 0–0.015 m^3/s (using four different stages). The upper bounds of these intervals are defined to avoid significant loss of the bed material due to splashing. The lower threshold for the fluidization number is set as low as possible while ensuring adequate fluidization. Similarly, the minimum bed height is established to ensure the effective functioning of the conveying section. In this study, a total of 48 experiments was performed, testing 16 unique combinations of three operational parameters. Each combination was replicated three times to ensure the robustness of the results.

4. Tracer concentration analysis: Analytical and modeling techniques

This section outlines the strategies used to derive the data from the analyses of the transient concentration profiles of tracer solids. Section 4.1 details the deconvolution of measured the transient tracer concentration profiles used to obtain the RTDs of the solids. Section 4.2 presents the application of a one-dimensional, transient, convection-dispersion model to describe the measured tracer concentration data by fitting the horizontal solids dispersion and velocity parameters. Section 4.3 presents the compartment model that is used to represent the measured data and thereby, determine the extent of the dead zones and mixing. Section 4.4 introduces the normalized mean-squared error metric, which allows comparison of the performances of the different analytical tools used in the current study.

4.1. Richardson-Lucy deconvolution technique

For each coil pair dataset, the Richardson-Lucy deconvolution algorithm [31,32] is applied iteratively to determine the RTD, E(t), that convolves the tracer concentration at Coil 1, $C_{in}(t)$, into the tracer concentration at any of the coils 2–4, $C_{out}(t)$. The algorithm quantifies the error by summing the absolute discrepancies between gradients of the input signal convoluted by means of the estimated system function and the initial signal.

This algorithm, which is also commonly used for signal restoration, is utilized to analyze concentration signals with the objective of reconstructing accurate concentration profiles from the observed input concentration signal C_{in}. Adapted for concentration signal analysis, the algorithm iteratively refines the estimated output concentration profile C_{out} based on an initial approximation and using maximum likelihood estimation based on Bayesian theory. Each iteration improves the estimate in response to the system's response function E, as shown in Eq. (9):

$$C(t)_{out,i+1} = C(t)_{out,i} \cdot \left(\left[\frac{C(t)_{in}}{C(t)_{out,i} \cdot E(t)} \right] \cdot E(t)_r \right) \tag{9}$$

Fig. 4a displays the RTD curves derived through deconvolution between Coil 1 and each of Coils 2 to 4 (for FN_{TZ}=3, H = 0.08 m, Q_{CZ} =

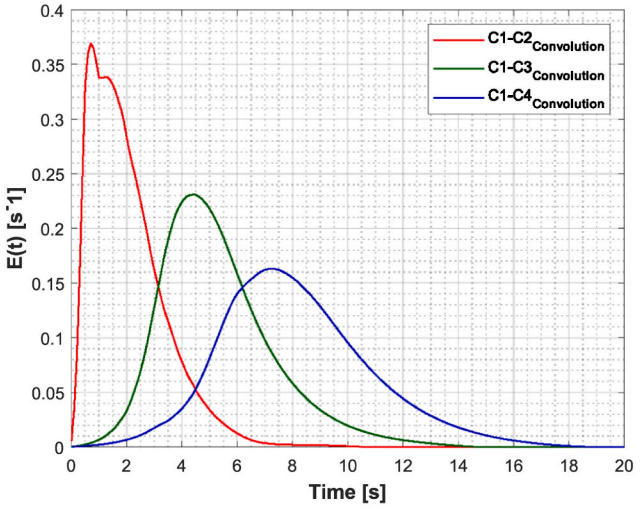

(a) E-curves for the domains comprised between Coil 1 and each of Coils 2–4, calculated with the deconvolution technique.

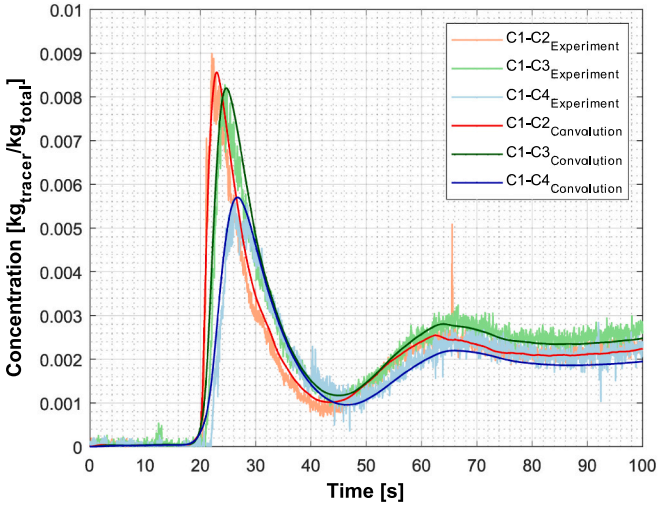

(b) Comparative analysis of experimentally acquired and convoluted transient profiles of the tracer concentration for Coils 2–4, validating alignment and data consistency.

Fig. 4. Richardson-Lucy deconvolution results and validation. Conditions: FN_{TZ} = 3, H = 0.08 m, Q_{CZ} = 0.0143 m^3/s.

0.0143 m^3/s). Note that the corresponding raw concentration profile data are presented in Fig. 3a. In the deconvolution process of this work, a low-pass filter is applied to the measurement data series, to remove experimental noise. To validate the methodology, the transient tracer concentrations obtained by convoluting the signal from Coil 1 with the calculated RTDs for Coils 2 to 4 are presented in Fig. 4b, together with the corresponding measurement data.

4.2. Convection-dispersion equation

The finite volume method [22] has been used to solve, through discretization, the convection-dispersion equation, expressed in its 1-dimensional (along the solids flow macroscopic direction) transient form, as in Eq. (4). A fully implicit discretization method was implemented, thereby ensuring stability and consistent time integration of the system. The hybrid differencing scheme integrates the precision of central differencing in uniform regions with the stability of upwind differencing in regions that feature steep gradients or discontinuities, making it the preferred approach. The modeled domain consists of the fluidized bed extending from the location of Coil 1 to the inlet of the solids-conveying section (see Fig. 1). Boundary conditions are defined at these two locations: at Coil 1, a transient Dirichlet condition is set by the measured tracer concentration, while at the inlet to the conveying section (which represents the outlet of the domain studied), a zero-gradient is imposed on the tracer concentration, representing a wall that is permeable to convection but not dispersion.

This work uses the convection-diffusion equation to determine its two governing parameters – the velocity and the dispersion coefficient – by fitting the calculated and measured transient concentration data at Coils 2, 3, and 4. This is achieved by minimizing an error function, as in Eq. (10), which compares the modeled transient curves of the tracer concentration, $C_M(t)$, with measurements, here represented by a 10th-order polynomial fit of the measured tracer concentration, $P(C_E(t))$. Initially, the raw concentration signal (Fig. 3a) is subjected to low-pass filtering to attenuate high-frequency noise and enhance the stability of subsequent calculations. However, careful attention is required to prevent over-filtering, which may eliminate significant signal components, particularly the characteristics of the concentration peak. Subsequently, a 10th-degree polynomial fitting is applied to achieve a smooth signal that retains the characteristic shape of the experimental curve while allowing gradient-based error analysis, which is crucial for the optimization procedure. Directly fitting a polynomial to the raw signal without prior filtering can lead to an inaccurate representation, as noise and high-frequency variations may obscure the underlying trend or significant features. Further details are provided in **Appendix F**.

This approach ensures that signal fluctuations are reduced to minimize their impacts on the error calculations, while the essential information and defining features of the curve are preserved, thereby maintaining the integrity of the data analysis. The error function employs a gradient-weighted squared error, prioritizing data-points that exhibit higher change rates. The variable 'n' in this context signifies the specific coil number. The error weightings for each of coils 2–4, W_{C_n}, are adjusted taking into account their specific SNRs.

$$E_C = \frac{1}{3} \times \sum_{n=1}^{3} \left\{ \left(\frac{\sum \left\{ \left| P\left(C_{E,n}(t)\right) \right| \times \left| P\left(C_{E,n}(t)\right) - C_{M,n}(t) \right|^2 \right\}}{\sum \left| P\left(C_{E,n}(t)\right) \right|} \right) \times W_{C_n} \right\} \tag{10}$$

Fig. 5 demonstrates the data processing used for determining the values of the velocity and dispersion coefficient for an example case. The measured and simulated transient tracer concentration curves at each coil are compared in Fig. 5a, in conjunction with the input signal from Coil 1. These simulations utilize the velocity and dispersion coefficient values, thereby minimizing the error. The data from all the coils clearly demonstrate the initial passage of the tracer batch, visible as pronounced peaks in the tracer signal. Coils that are located further from the injection point show wider peaks, indicative of greater dispersive mixing. Subsequently, a decrease in tracer concentration is observed, followed by a second, less-prominent peak, which represents a subsequent traversal of the tracer batch after completion of a circulation loop around the unit. Ultimately, the curves exhibit a gradual transition to a stable state, in which the solids tracer is uniformly dispersed throughout the bed, reaching a consistent concentration. In Fig. 5b, an error contour plot is employed to demonstrate the identification of the optimal values for the velocity and dispersion coefficient. The two error bars (for horizontal solids velocity and solids dispersion) indicate the extents of uncertainty associated with these values, marking the ranges for a 5% increase of the error value.

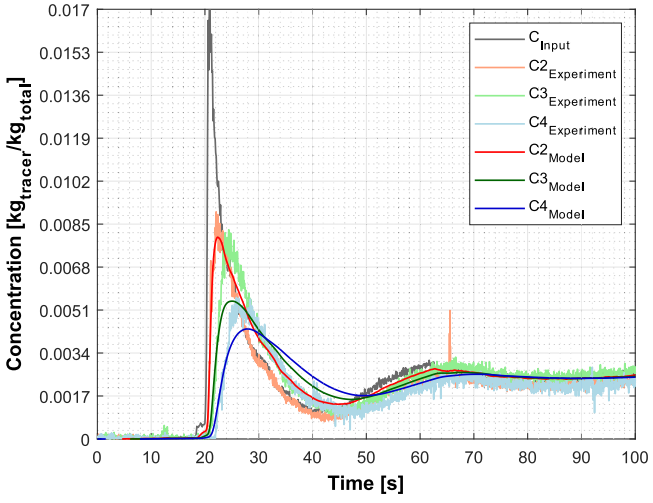

(a) Measured and modeled transient concentrations of the solids tracer.

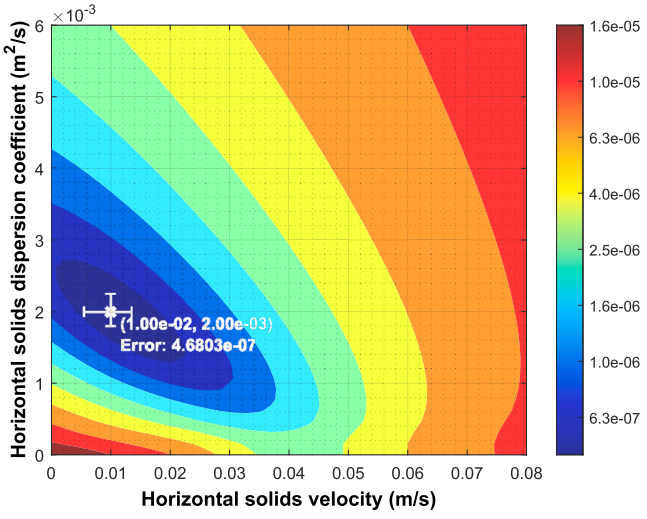

(b) Error surface plot [see Equation (10)].

Fig. 5. Model validation and use for determination of the solids velocity and dispersion coefficient. Conditions: $FN_{TZ} = 3$, H = 0.08 m, $Q_{CZ} = 0.0143$ m^3/s.

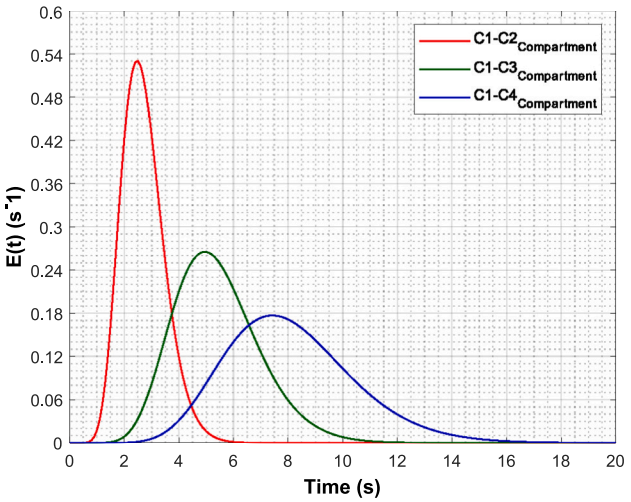

(a) E-curves for the domains comprised between coil 1 and each of Coils 2–4.

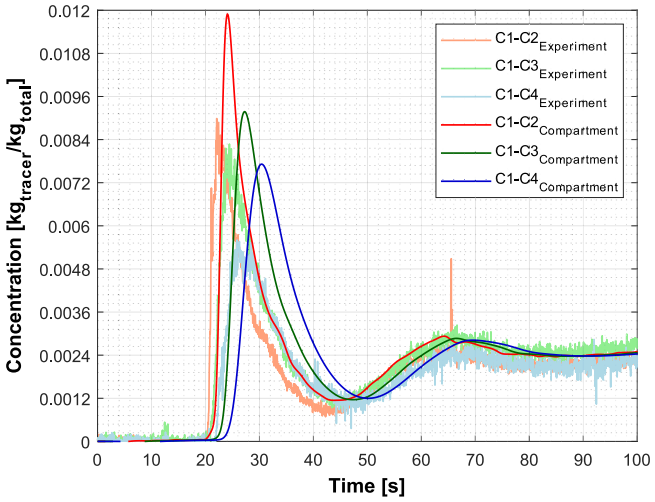

(b) Comparative analysis of experimental and model-derived tracer concentration profiles for Coils 2–4.

Fig. 6. Compartment model fitting results and validation. Conditions: $FN_{TZ} = 3$, $H = 0.08$ m, $Q_{CZ} = 0.0143$ m^3/s.

4.3. Optimized parameter extraction via compartment modeling

A non-linear optimization code routine is implemented to fit the compartment model parameters [see Eq. (6)]. The tracer concentration signal from Coil 1 is treated as the input signal to the model, while model parameter fitting is used to minimize the error between the modeled and measured signals for output Coils 2–4. The adjusted parameters are the dead zone index (which measures the extent of stagnant flow regions), the mean residence times in the CSTRs and PFR components, and the number of CSTRs in series (representing the flow characteristics and extent of mixing). A multi-start optimization approach is utilized to overcome the challenge of multiple local optima by running the optimization process multiple times with varied starting points, thereby increasing the chances of identifying the global optimum [33]. The chosen solution is based on the minimum value of the objective function across all runs, ensuring the best fit between the model predictions and experimental data.

Fig. 6a presents an example of RTD curves obtained from compartment model fitting between Coil 1 (input, $C_{in}(t)$) and Coils 2–4 (output, $C_{out}(t)$). For the same experiment, Fig. 6b displays the transient tracer concentrations of the output signals, determined by applying the fitted parameters to Eq. (6), alongside the corresponding measurement data.

4.4. Error metric

Analyses of the different solids flow representations considered in this work are carried out by comparing the convection-dispersion model and the compartment model through examining the concentration curves that they produce against those obtained from experiments. This comparison involves a normalized mean squared error (NRMSE) metric approach, as detailed in Eq. (11). This is calculated by dividing the root mean squared error (RMSE) by the difference between the maximum concentration value observed in an experiment $C_{E,Max}$ and the concentration level reached when the tracer has fully dispersed or uniformly distributed in the bed $C_{E,ss}$.

$$Error = \frac{\sqrt{\frac{1}{n}\sum_{i=1}^{n}\left[C_M(t) - C_E(t)\right]^2}}{C_{E,Max} - C_{E,ss}} \tag{11}$$

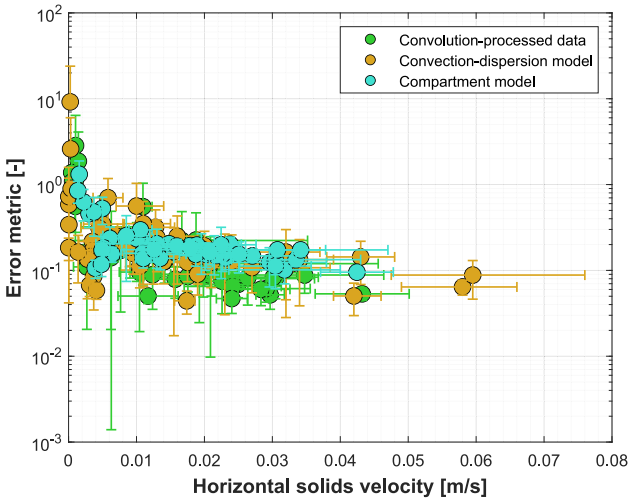

Fig. 7. Assessment of the error metric [Eq. (11)] derived from each of the three analytical methods used.

5. Results and discussion

Section 5.1 provides a comparison and discussion of the errors obtained using: 1) deconvolution of the experimental signals (Section 5.2); 2) the 1D convection-dispersion model (Section 5.3); 3) and the compartment model (Section 5.4). Section 5.2 employs the statistical method of moments to analyze the RTD curves derived through deconvolution of the measurement data. In Section 5.3, the values for the solids velocity and dispersion coefficient obtained through fitting to the convection-dispersion model are shown and discussed, together with the ability of the convection-dispersion framework to describe the cross-sectional solids flow that is established. Section 5.4 utilizes compartment modeling to explore the presence of dead zones, as well as to identify and examine the extents of the different modes of mixing.

5.1. Comparison of data processing methods

Fig. 7 utilizes the error metric [see Eq. (11)] to compare the accuracies of the two model approach methodologies in describing the transient concentration profiles of the tracer solids. Furthermore, the

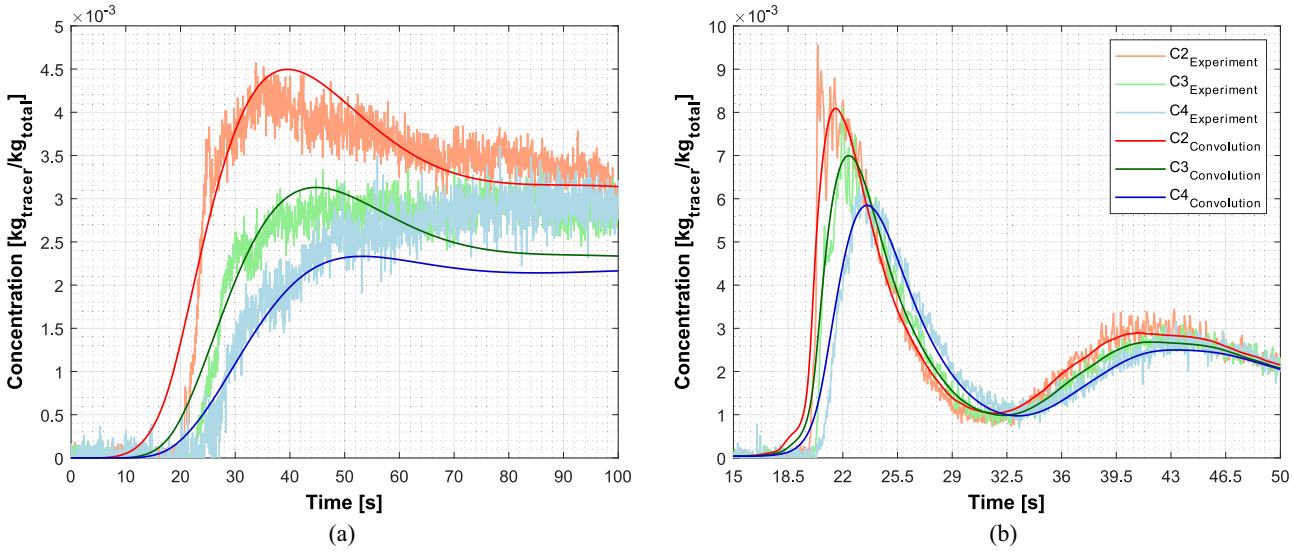

Fig. 8. Transient profiles of the tracer concentrations. Shown are the measured (noisy) and convolution-derived (smooth) values at: a) low solids velocity (Q_{CZ} = 0.0026 m^3/s), and b) high solids velocity (Q_{CZ} = 0.0143 m^3/s). Conditions: FN_{TZ} = 3, H = 0.08 m.

error for the convoluted solids concentration profiles generated by the deconvolution technique is plotted, so as to gain an understanding of its accuracy and, thereby, the reliability of the data derived from it. The error values, which are represented by vertical bars in Fig. 7 that denote the disparities between the experimental concentration and the model output (averaged for three coils), are plotted against the respective solids velocity values obtained for the varying set of operational conditions tested in this study. The uncertainty associated with the solids velocity is indicated by the horizontal bars in Fig. 7. The plotted data illustrates that the three analytical methods exhibit comparable error levels and follow a common trend: higher errors relative to the measured data are evident at low solids velocities. As the solids velocity increases, the error values gradually decrease and eventually plateau, stabilizing at approximately 10^{-1} for u_S>0.1 m/s.

5.2. Deconvolution of experimental data

The Richardson-Lucy deconvolution technique (**Section 4.1**) is utilized to derive the RTD curves from coil pairs. In order to assess the performance of the technique, the calculated RTD curves are used to convolute the input coil (Coil 1) concentration signal into a reconstruction of the concentration signal of the output coils (Coils 2–4), which can be compared to the measured one. Fig. 8 presents such comparisons for a low and a high solids velocity. There is a good agreement between the convolution data and measurements at high solids velocities, while there are discrepancies at low solids velocities. These discrepancies primarily stem from the violation of the key assumptions made in the Richardson-Lucy deconvolution technique. First, the assumption of a point-source injection is compromised, as sluggish flow conditions can lead to non-uniform tracer dispersion. Second, the system's linearity assumption is challenged, given the emergence of nonlinearity for the flow dynamics, including stagnant zones and backmixing. Third, the assumption of homogeneous and well-mixed flow conditions is not met in scenarios with low solids velocities, resulting in flow heterogeneity and variations in tracer dispersion that the deconvolution method struggles to capture accurately. However, despite the deviations observed at low solids velocities, the reconstructed concentration curves are considered to agree reasonably well with the experimental data.

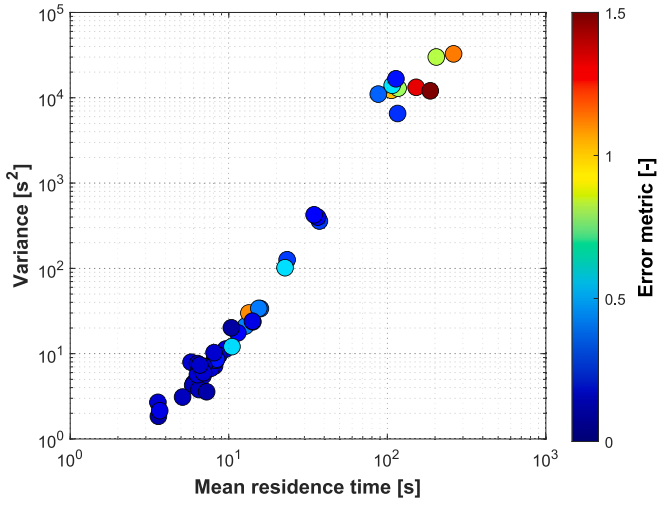

Fig. 9. Method of moments analysis of the RTD curve post-deconvolution with error magnitude comparison.

The decreased accuracy of the convolution technique in describing experimental data at low solids velocity (corresponding to a longer mean residence time) is also seen in Fig. 9. The color-coded scheme illustrates the relative minimum square error between the reconstructed tracer concentration and the measured data for all the tested cases.

5.3. Convection-dispersion model

Fig. 10 shows the values for the horizontal solids velocities (Fig. 10a) and dispersion coefficients (Fig. 10b) obtained from the fitting of the convection-dispersion model to the experimental tracer concentration curves. These figures show the data for the 16 different conditions tested, which involved varying the bed height, *H*, fluidization number, FN_{TZ}, and volumetric flow rate of air fed to the solids-conveying zone, Q_{CZ}. The error bars represent the standard deviations obtained from three replicates of each experimental condition. Fig. 10a and Fig. 10b demonstrate that both the solids velocity and the dispersion coefficient increase in relation to the three operational parameters. The regression analysis, illustrated in Fig. 10c, quantifies the degree of influence that each operating parameter exerts on the model's extracted parameters, namely the 'solids velocity' (represented by blue bars) and the 'solids dispersion coefficient' (indicated by orange bars), using factorization values. This analysis highlights that the primary factor affecting the

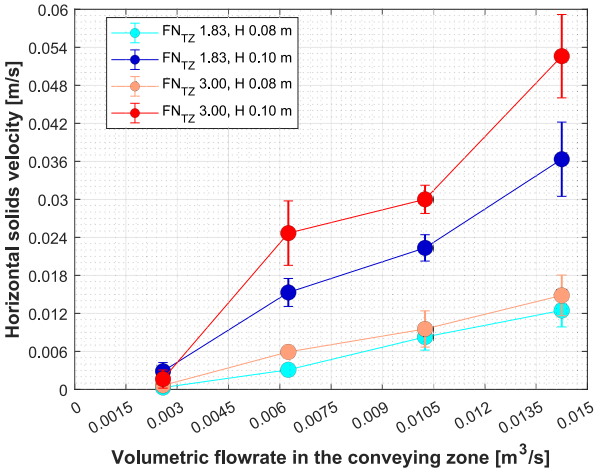

(a) Horizontal solids velocity as a function of the operational parameters.

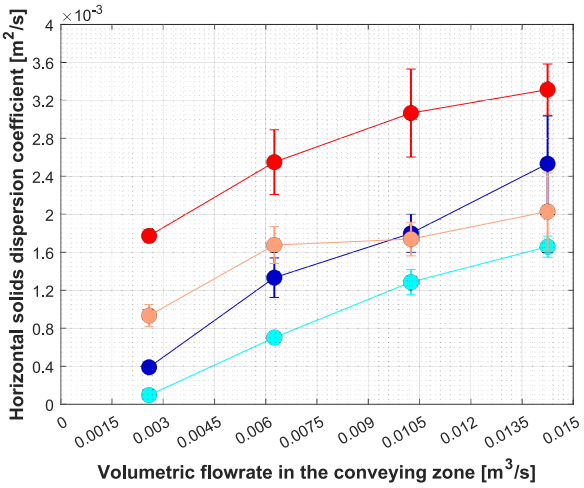

(b) Horizontal solids dispersion coefficient as a function of the operational parameters.

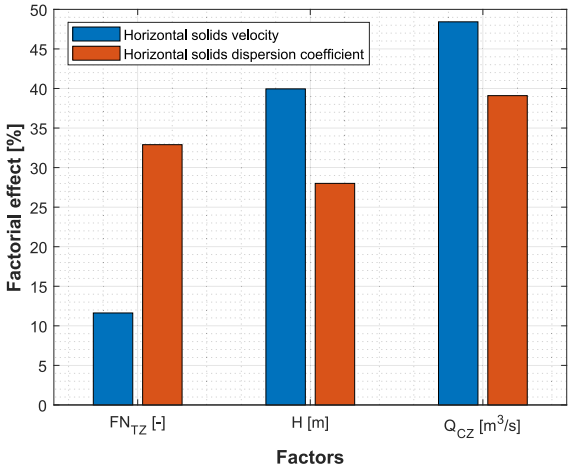

(c) Relative impacts of the three operational parameters varied in this work.

Fig. 10. Impacts of the operational parameters on the horizontal solids velocities and dispersion coefficients derived from the convection-dispersion model.

solids velocity (48%) is the airflow driving the solids-conveying section. In addition, the bed height has a significant impact (40%) on the solids velocity, mainly because an increase in bed height increases the solids-conveying section, resulting in an increased solids velocity. The fluidization number also influences the solids velocity, albeit to a lesser degree (12%), whereby an increase in the fluidization velocity results in greater voidage and, consequently, reduced friction in the solids circulation flow. The horizontal solids dispersion coefficient is primarily influenced (39%) by the airflow fed into the conveying section. Furthermore, the fluidization number and bed height have considerable impacts on the horizontal dispersion of solids, accounting for 34% and 27%, respectively. These findings align with those of previous studies [34] correlating these effects to the enhanced bubble flow and increased size that accompany an increased solids flowrate.

Fig. 11 displays the pairs of u_S-D_S values from all the experimental runs, encompassing the three repetitions for each operational case. The chart employs color coding to distinguish between different experimental conditions. The error bars represent the levels of certainty of the plotted values, indicating the range of values that result in a 5% increase of the calculated error, as per Eq. (10). It is noteworthy that there is a strong correlation between the solids horizontal dispersion and the solids horizontal velocity, which can roughly be described as linear ($r = 0.804$). Thus, when the bed height and fluidization velocity are constant, the introduction of a horizontal solids crossflow notably enhances the solids dispersion in the direction of the crossflow. One hypothesis for this observation is that the bed-wall friction creates shear mixing within the solids crossflow, which increases the solids back-mixing in the horizontal direction and, thus, contributes to the dispersive term that accounts for the mixing. As seen, in scenarios with no solids circulation within the system, i.e., $u_S = 0$, an increase in either bed height or fluidization number clearly enhances the horizontal solids dispersion. This observation aligns with previous research on stationary (i.e., without solids crossflow) BFBs [10]. However, as the solids velocity increases, the impact of bed height on the solids dispersion becomes less-noticeable, whereas the influence of fluidization velocity persists.

The increase in solids velocity that affects dispersive mixing has significant implications for reactor design and scale-up. This is particularly evident when enhancing the velocity of the solids crossflow to emulate a plug flow pattern. However, as demonstrated in Fig. 11, the horizontal solids dispersion coefficient (D_S) increases with solids velocity (u_S), making it more difficult to maintain a high Péclet number (Pe) and, consequently, a more-pronounced plug flow behavior (for further details, see **Appendix H**).

Fig. 12 complements the preceding figure by displaying the horizontal solids dispersion coefficient in relation to the solids velocity, with the color temperature indicating the relative error values between the modeled and experimental data, as defined by Eq. (10). It is evident that conditions with low solids velocities yield higher errors, whereas the

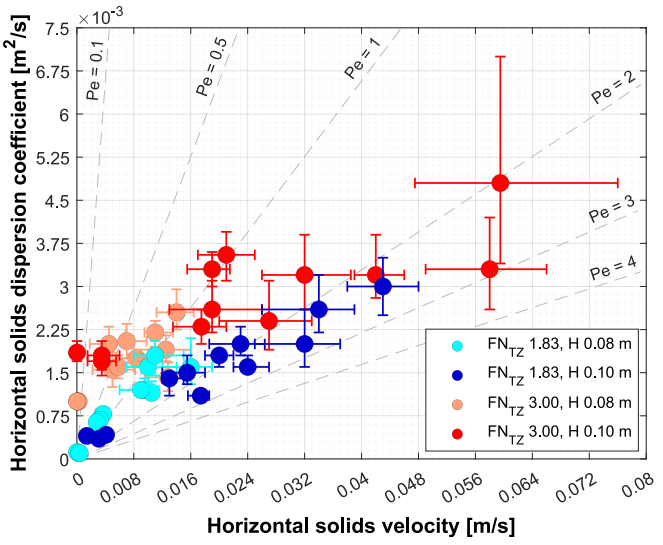

Fig. 11. Horizontal solids dispersion coefficients for different horizontal solids velocities, bed heights, and fluidization numbers. The bars indicate the value certainty levels by marking the value ranges that yield an error increase of < 5%. The dashed lines indicate the Péclet numbers (*Pe*).

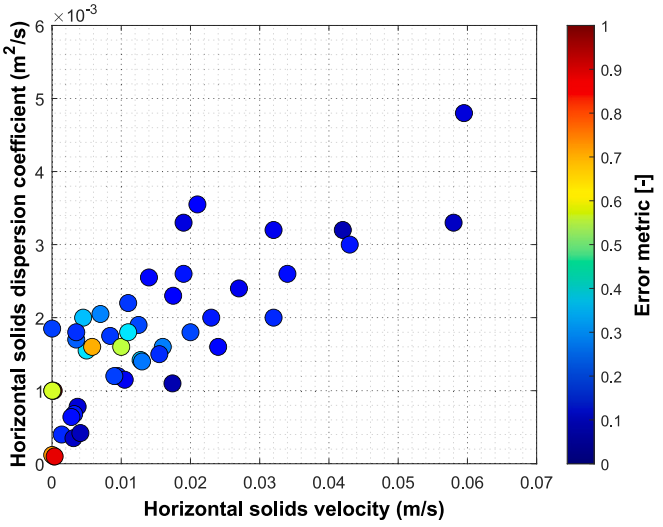

Fig. 12. Analyzing the error magnitude in the parameter estimations with the 1D transient convection-dispersion model.

convection-dispersion model effectively describes scenarios with higher solids velocities. The discrepancies observed at low solids velocities can be attributed to the increased influences of non-ideal characteristics on the dispersive mixing mechanism. These errors are likely the result of uneven fluidization caused by factors such as wall effects and the way in which the plate distributor is assembled. The distributor, which is composed of welded pieces, creates inconsistencies in the fluidization patterns across the transport zone, thereby disrupting the uniform flow of the fluidizing medium due to the welding points.

5.4. Compartment model

As mentioned above, the compartment modeling fits the outlet concentration profiles from the compartment models to experimental profiles with adjustment of the following essential model parameters: the dead zone index (i_d); the mean residence times in the CSTR (τ_{CSTR}) and PFR (τ_{PFR}) components; and the number of series-coupled tank reactors in the well-stirred compartment (N_{CSTR}). For all the cases, the model fitting resulted in negligible values for the PFR component. Consequently, this component is omitted from the subsequent analysis.

Fig. 13 illustrates the influence of operational conditions on the fitted values of the dead zone index (Fig. 13a) and the number of CSTR tanks (Fig. 13b). The dead zone index, as shown in Fig. 13a, exhibits a declining dependency on increasing the value of the three operational parameters investigated: fluidization number, bed height, and the rate of conveyed solids. Notably, the latter two parameters differ from intuitive expectations. In stationary bubbling beds, taller beds usually have reduced gas-solids mixing due to a higher bed-to-distributor pressure drop ratio and the growth of larger bubbles. This pattern is also evident at low solids circulation rates when operating under conditions of low fluidization velocity. However, the measured data indicates that a significant solids crossflow minimizes stagnant zones more effectively in taller beds than in shallower ones. In addition, there is an increased solids crossflow at a constant bed height, and the fluidization velocity more effectively reduces the stagnant zones. However, the methodology employed in this study does not allow for evaluation of the different stagnation mechanisms such as wall/distributor-related or in-bed dead zones. Given that an increase in solids crossflow yields stronger gradients of the solids velocity at the walls and the distributor, it seems plausible that such stagnant zones become activated, but in-bed solids stagnation can similarly vanish with increased crossflow. Regarding the second model parameter, the solids residence time in the CSTR section is directly derived from a mass balance relationship that covers the extent of the dead zones and the rate of solids crossflow. Therefore, its specific values are not elaborated upon in this discussion.

The number of CSTRs arranged in series exhibits a notable upward trend, primarily driven by the rate of solids conveyance. This trend indicates a general transition of the solids crossflow from a homogeneous mixing pattern that is typical of a CSTR to a plug flow pattern. This aligns with the findings presented in Fig. 11, which demonstrate an overall increase in the *Pe* number with solids velocity. However, it is essential to note that there is a saturation trend at higher solids velocity values.

To understand better the influence of operational parameters on the regression model following the compartment model fitting for the three variables, an additional regression analysis is conducted. This process involves deriving the factorial effect, expressed in terms of percentage, for each operating parameter. Fig. 13c presents a quantitative evaluation of the interplay between the model and operational parameters for the setup and conditions tested. It is evident that the primary factor influencing the model parameters is the gas flow rate fed to the solids-conveying zone, Q_{CZ}, which accounts for approximately 60%–75% of the variation. In contrast, the sensitivity to variations in bed height and fluidization number is less-pronounced, accounting for a weaker influence in the range of 10%–26%.

Fig. 14 shows the analysis based on applying the method of moments to the RTD curves derived from the defined compartment model. The figure highlights that this error tends to increase as the solids velocity decreases, which corresponds to longer mean residence times. The increased disparity observed at lower solids velocities may be attributed to the greater probability of solids back-mixing, a phenomenon that was

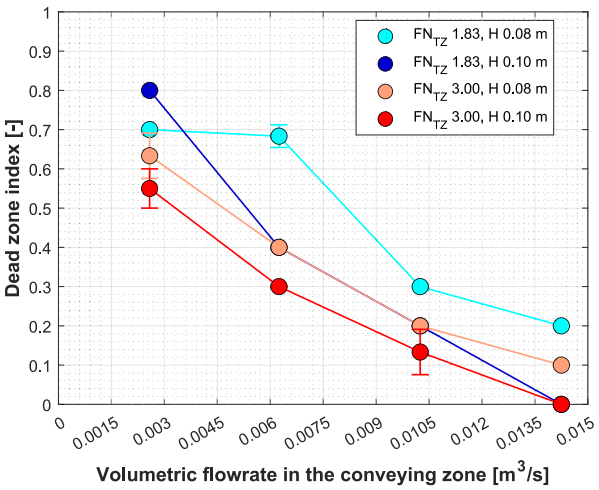

(a) Dead zone index as a function of the operational parameters.

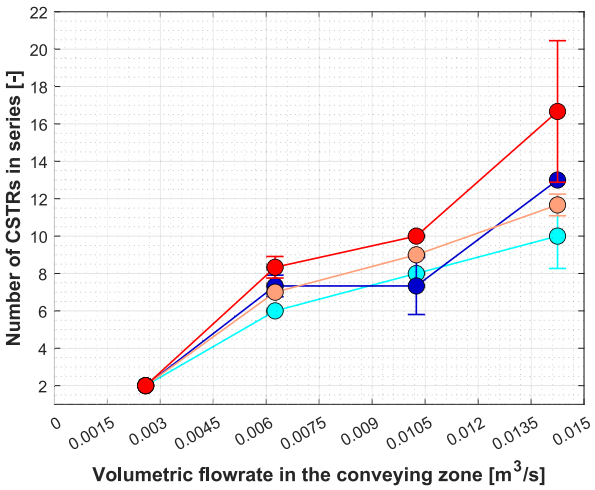

(b) Number of CSTRs in series as a function of the operational parameters.

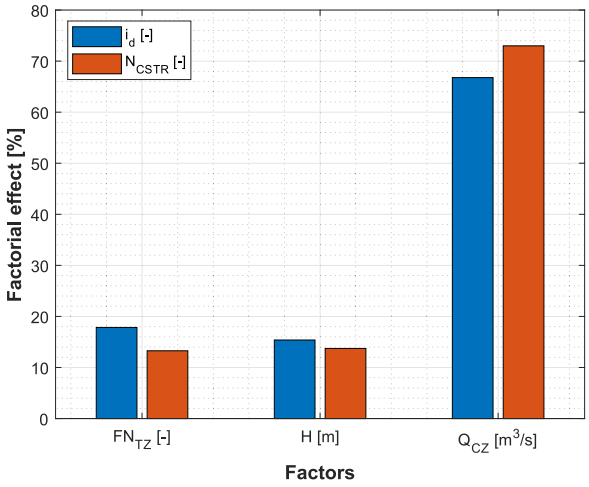

(c) Relative impacts on the fitted variables of each varied operational parameter.

Fig. 13. Impacts of operational conditions on the variables obtained after optimization of the compartment model fitting.

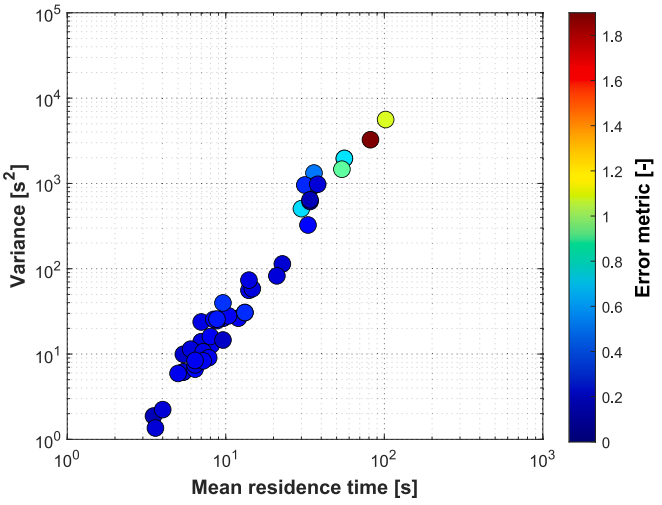

Fig. 14. Statistical moments in the RTD curves obtained from the compartment model, alongside the errors in the tracer concentration curves compared to the measurements.

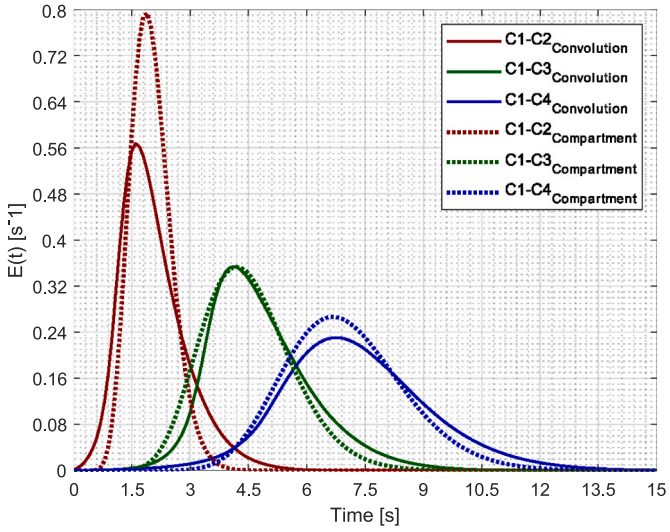

Fig. 15. Residence time distributions derived from the deconvoluted measurement data (solid lines) and the compartment model (dotted lines). Conditions: $FN_{TZ} = 3$, $H = 0.10$ m, $Q_{CZ} = 0.0143$ m^3/s.

not considered in the model layout. This back-mixing can occur due to splashing or the presence of recirculation zones.

Fig. 15 compares the RTD curves derived from the deconvoluted measurements with those derived from the compartment model. The RTD curves derived from the compartment model are in good agreement with those obtained from the deconvoluted measurement data. However, as shown here, minor disparities, such as a slightly higher variance, are observed in the compartment-model-derived RTD curves. These discrepancies underscore the constraints that are inherent to the simplified model representation, which, for example, is unable to encompass fully the intricate flow dynamics features, such as back-mixing and recirculation.

6. Conclusions

This work studies the flow characteristics of the solids crossflow in a BFB. The experimental setup consists of a unit in which a horizontal flow of fluidized solids is forced to circulate in a closed loop. By employing magnetic solids tracing (a non-intrusive measurement technique), the transient concentrations of injected batches of solids tracers can be sampled at different locations along the solids circulation loop. In the experimental series, three operational parameters are varied: fluidization velocity; bed height; and conveyed solids flow. The study explores three methodologies for analyzing the measurement data: i) deconvolution of the measured transient profiles of the tracer concentrations; ii) fitting of the measurements to a convection-dispersion model; and iii) fitting of the measurements to a compartment model.

The three methods for analyzing the solids flow show good alignment with the experimental data and exhibit similar levels of discrepancy in their fits. The most significant discrepancies are observed for cases with low solids velocities, although this decreases gradually to a lower baseline for solids velocities above 0.01 m/s.

The deconvolution of the measured tracer concentration signals yields valuable insights into the dynamics and solids flows within fluidized beds, as represented by the characteristic RTD of the solids. The fitting of the experimental data to a convection-dispersion model reveals a strong and roughly linear relationship between the horizontal solids dispersion coefficient (1×10^{-4}–5×10^{-3} m^2/s) and the solids velocity (3×10^{-5}–6×10^{-2} m/s). Consequently, the Péclet number is observed to increase linearly with increased velocity. Thereafter, the curve flattens out for the highest velocities employed. This suggests that attaining a plug flow pattern for the solids crossflow by means of increased velocity may not be certain. The fitting of a compartment model to the measurements (by adjusting the dead zone index, residence times in the CSTR and PFR, and the number of tank reactors) reveals a decrease in the dead zone index with increases in the solids crossflow, bed height, and fluidization velocity.

Nomenclature

Ar	Archimedes number, [−]
C	Concentration, [kg/m^3]
D_S	Horizontal solids' dispersion coefficient, [m^2/s]
d_{32}	Sauter mean diameter, [μm]
d_S	Particle diameter, [μm]
$E(t)$	Exit age distribution, [−]
E_C	Gradient-weighted squared error used for the convection-dispersion model, [−]
FN_{TZ}	Fluidization number in the transport zone, [−]
H	Fixed bed height, [m]
i_d	Dead zone index, [−]
k	Calibration factor of inductance, [−]
L	Length, [m]
M	Mass of solids tracer injected, [kg]
N_{CSTR}	Number of reactors in tank-in-series component of the compartment model, [−]
Q	Volumetric flowrate of solids tracer, [m^3/s]
Q_{CZ}	Volumetric flowrate in the solids-conveying zone, [m^3/s]
SNR	Signal-to-noise ratio, [dB]
t	Time, [s]
u_0	Fluidization velocity, [m/s]
u_{mf}	Minimum fluidization velocity, [m/s]
u_S	Horizontal solids' velocity, [m/s]
V	Volume, [m^3]
W_{C_n}	Error weightings for the coils, adjusted according to the signal-to-noise ratio, [−]
x	Horizontal position, [m]
Z	Background inductance of the coil, [H]
Z_0	Measured inductance with the tracer material, [H]
ρ_B	Bulk density, [kg/m^3]
ρ_F	Density of gas, [kg/m^3]
ρ_S	Density of solid particles, [kg/m^3]
μ_F	Gas viscosity, [Pa•s]
τ	Mean residence time, [s]
σ^2	Variance, [s^2]

CRediT authorship contribution statement

Munavara Farha: Writing – original draft, Validation, Methodology, Investigation, Formal analysis. **Diana Carolina Guío-Pérez:** Writing – review & editing, Supervision, Methodology, Conceptualization. **Filip Johnsson:** Writing – review & editing. **David Pallarès:** Writing – review & editing, Supervision, Funding acquisition, Conceptualization.

Declaration of competing interest

The authors declare the following financial interests/personal relationships which may be considered as potential competing interests:

Munavara Farha reports financial support was provided by Swedish Energy Agency. If there are other authors, they declare that they have no known competing financial interests or personal relationships that could have appeared to influence the work reported in this paper.

Data availability

Data will be made available on request.

Acknowledgements

The authors acknowledge the financial support received from the Swedish Energy Agency within the framework of project 51182-1 – *Thermochemical poly-generation in heat and power plants*. The contribution of RISE Sensor Systems is also acknowledged, which made possible the development of the Magnetic Solids Tracing system used in this work.

Appendix A

Calibration-induced uncertainties are quantified via the standard deviation of the residuals from the linear fit predictions, as shown in Eq. (A1). The analyses focus on two key parameters: fluidization number, and bed height.

$$U_k = \frac{\sqrt{\frac{1}{N-1}\sum_{i-1}^{N}\left(k - k_{pred}\right)^2}}{\sqrt{\sum_{i-1}^{N}\left(C_{t,i} - \overline{C_t}\right)^2}} \tag{A1}$$

Fig. A.1 presents the coil calibration data across a spectrum of operational conditions. The primary *y*-axis (bar graph) represents the calibration constant, while the secondary *y*-axis (red markers) represents the quantified calibration uncertainty.

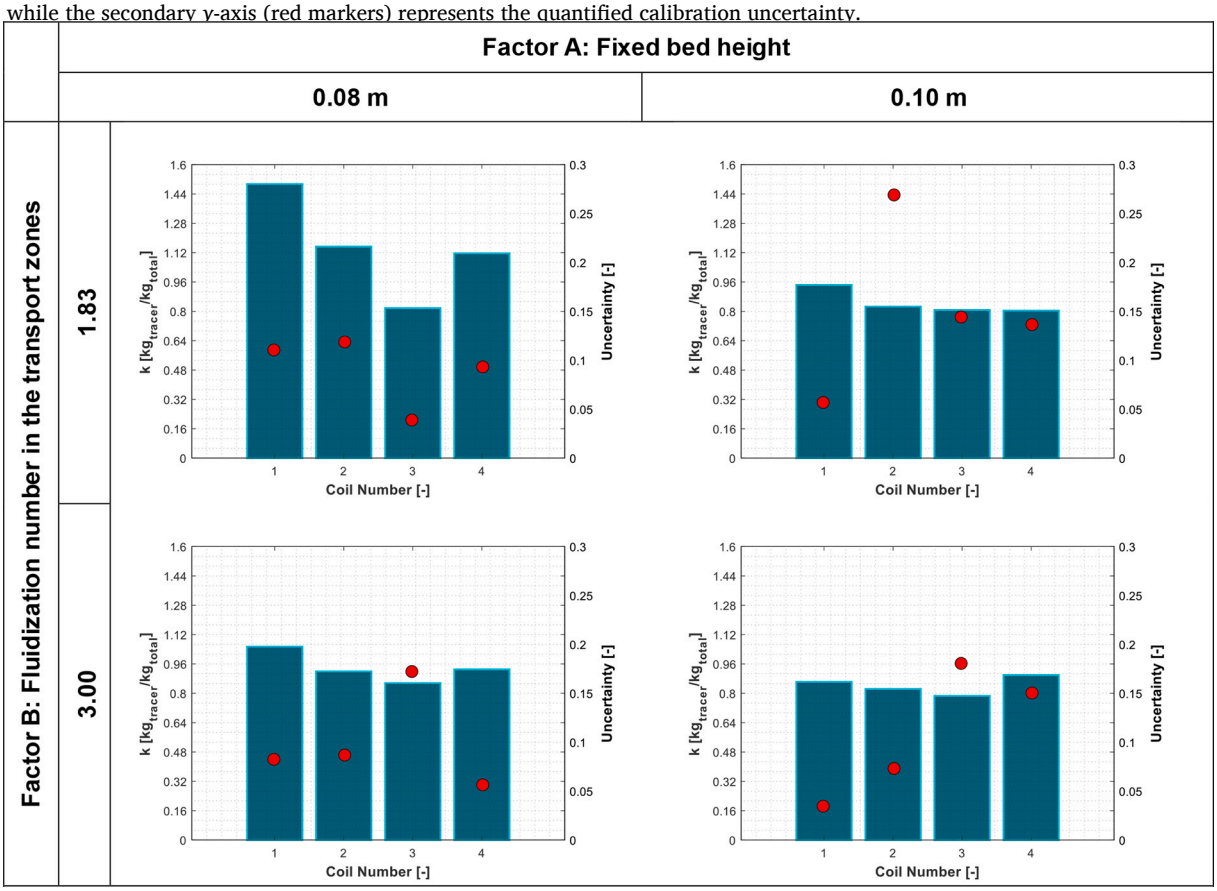

Fig. A.1. Quantification of calibration 'k' uncertainty across the impedance coils.

Appendix B

Fig. A.2**a** showcases the results of the Richardson-Lucy deconvolution over 50 iterations. The red solid line represents the experimental data, the blue dashed line denotes the convolution values for each iteration, and the green solid line signifies the convolved profile at the optimal iteration.

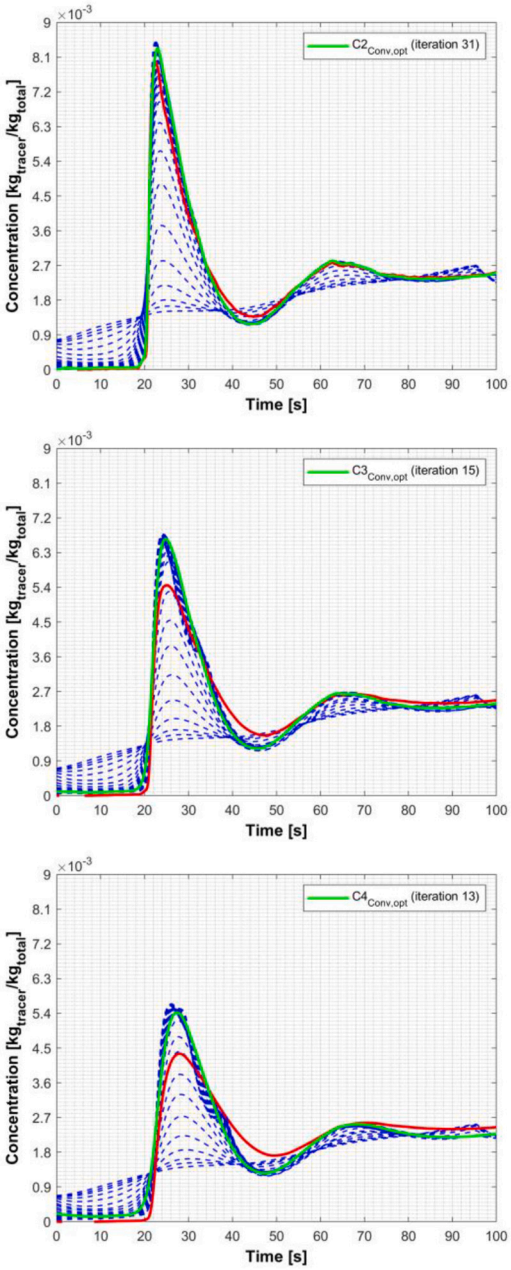

(a) Concentration-time profiles for Coils 2–4, illustrating the Richardson-Lucy deconvolution results over 50 iterations, with the optimal iteration convolution indicated in green.

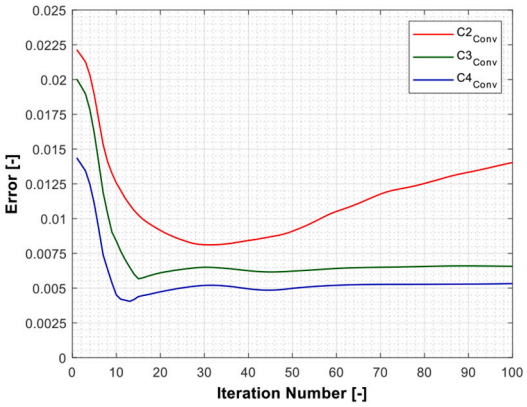

(b) Error progression for Richardson-Lucy deconvolution across Coils 2–4, plotted over a maximum of 100 iterations.

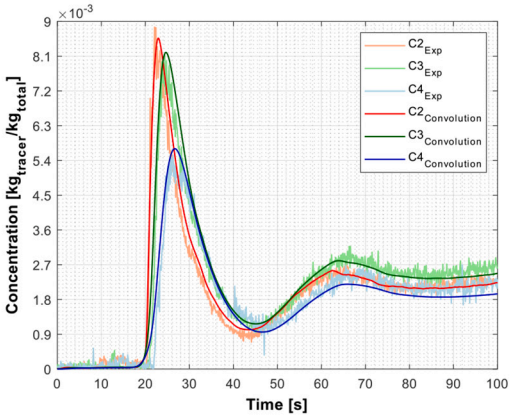

(c) Comparative analysis of experimentally acquired and convoluted concentration-time profiles for Coils 2–4, validating the alignment and data consistency.

Fig. A.2. Richardson-Lucy deconvolution results and validation for Coils 2–4 through concentration-time profiling, error progression, and experimental versus convoluted data comparisons. Conditions: $FN_{TZ} = 3$, $H = 0.08$ m, $Q_{CZ} = 0.0143$ m^3/s.

As shown above, the coils selected for the analysis show that the iteration that exhibits the least error is employed for the $E(t)$ curve computation. Fig. A.2**b** depicts the convergence behavior of the deconvolution process for Coils 2–4, quantifying the error over a series of 100 iterations. The optimal iteration is determined based on the minimal error between the experimental data and the deconvoluted concentration profile.

Appendix C

Fig. A.3–Fig. A.6 illustrate the concentration profiles alongside their corresponding error surface plots, which have been fitted using the 1D-transient, convection-dispersion model. These plots demonstrate the behaviors of the horizontal solids velocity and the solids dispersion coefficients under varying operational conditions characterized by FN_{TZ} values of 1.83 and 3, respectively. With increasing severity of operational constraints, there is a corresponding increase in the coupled parameter values. The error surface plots, as exemplified in Fig. A.4 and Fig. A.6, offer a quantitative assessment of the model efficacy across the parameter domains and aids in the identification/optimization of key variables.

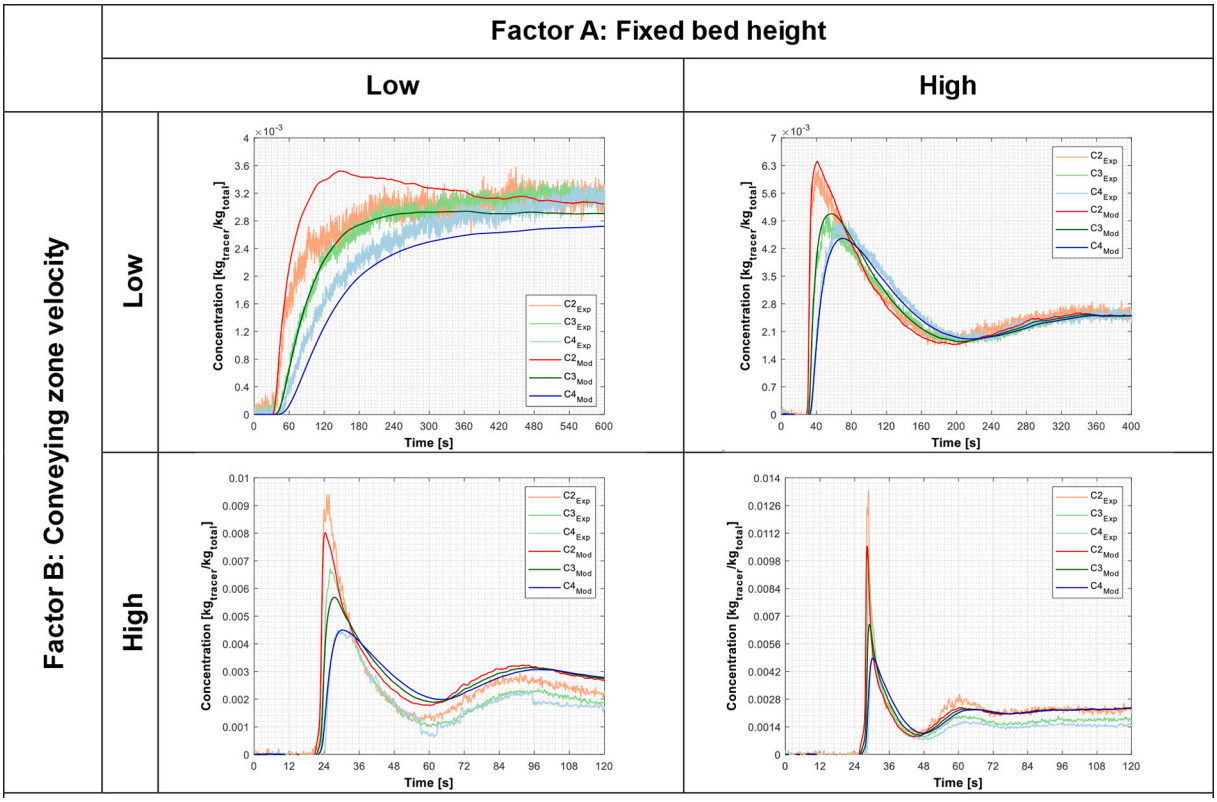

Fig. A.3. Model fit with experimental data for the operational condition of $FN_{TZ} = 1.83$.

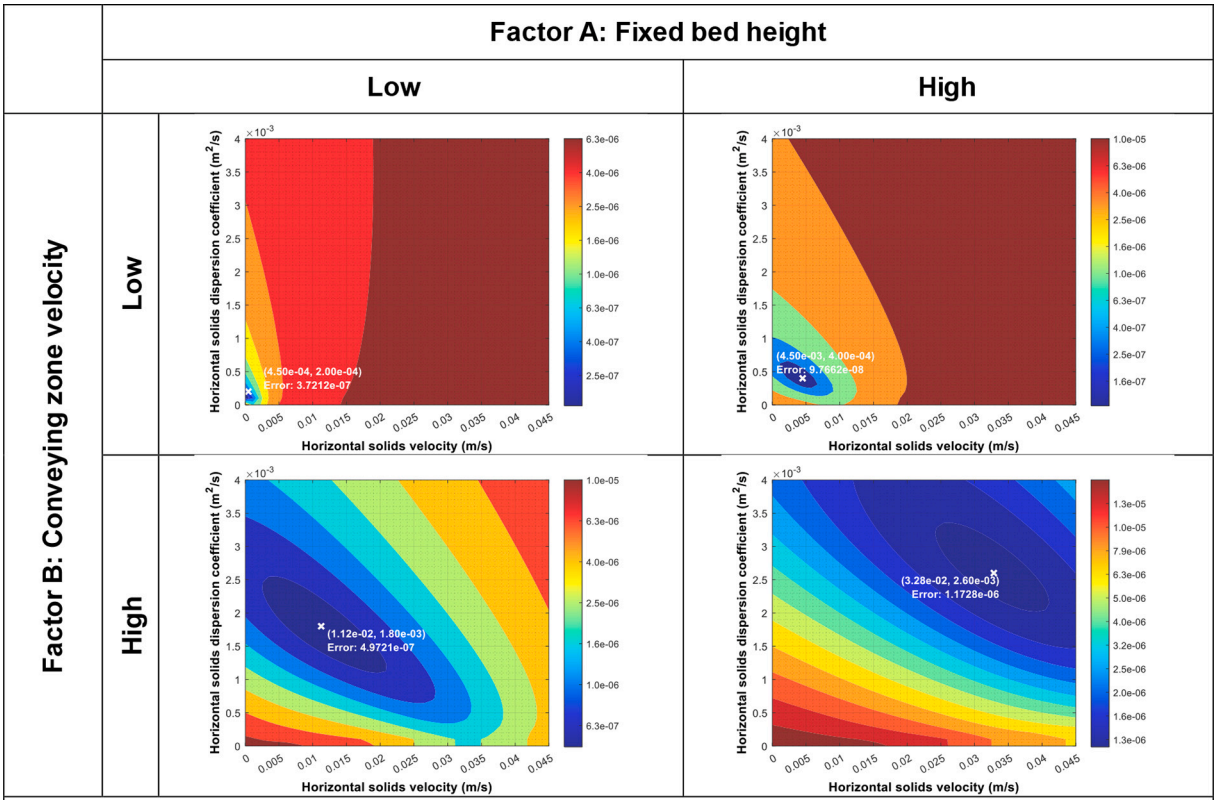

Fig. A.4. Error surface plots depicting the parameter interplay from model fitting, showcasing the results at extreme operational parameters with $FN_{TZ} = 1.83$.

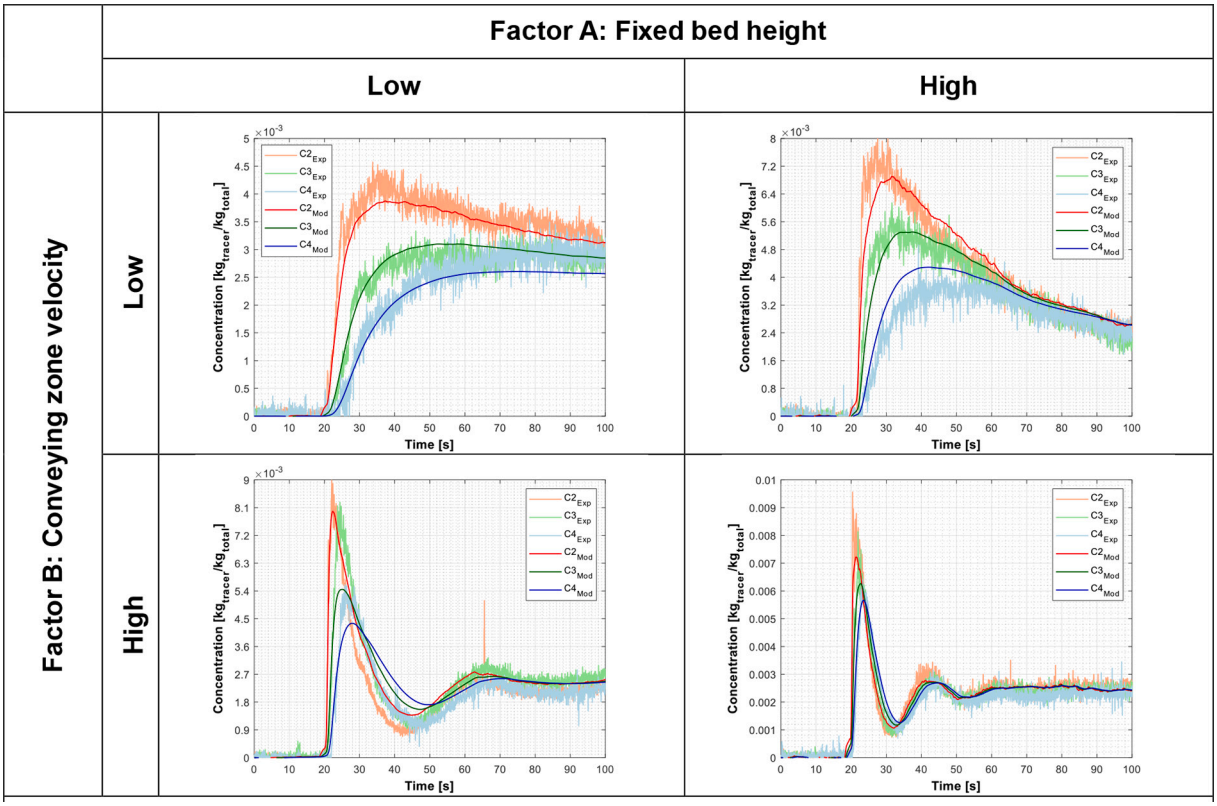

Fig. A.5. Model fit with experimental data for the operational condition of $FN_{TZ} = 3$.

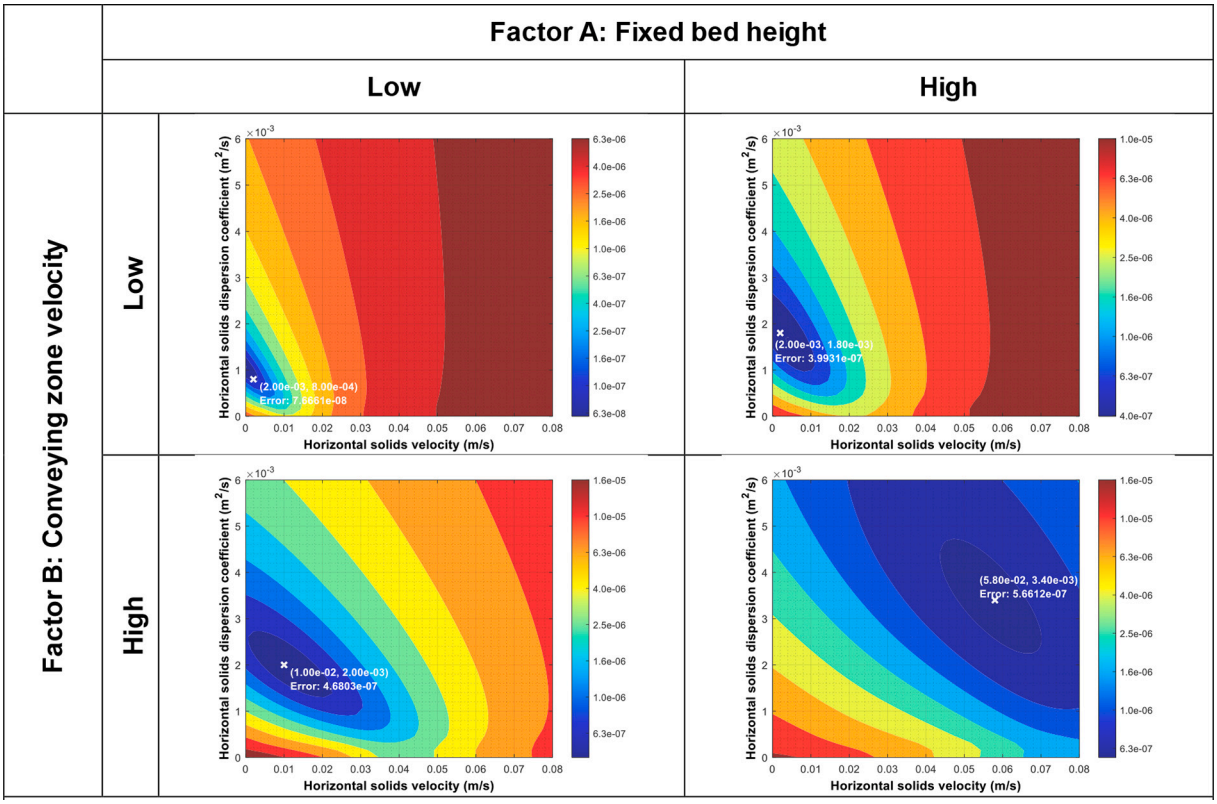

Fig. A.6. Error surface plots depicting the parameter interplay from model fitting, showcasing the results at extreme operational parameters with $FN_{TZ} = 3$.

Appendix D

Fig. A.7 presents the regression results, along with the main effects plots attained for the horizontal solids velocity and horizontal solids dispersion coefficient.

The regression models for both response variables are shown below:

$$u_S = -0.08764 + 0.00408\,FN_{TZ} + 0.8199\,H + 2.279\,Q_{CZ}$$

$$D_S = -0.005556 + 0.000886\,FN_{TZ} + 0.04412\,H + 0.1412\,Q_{CZ}$$

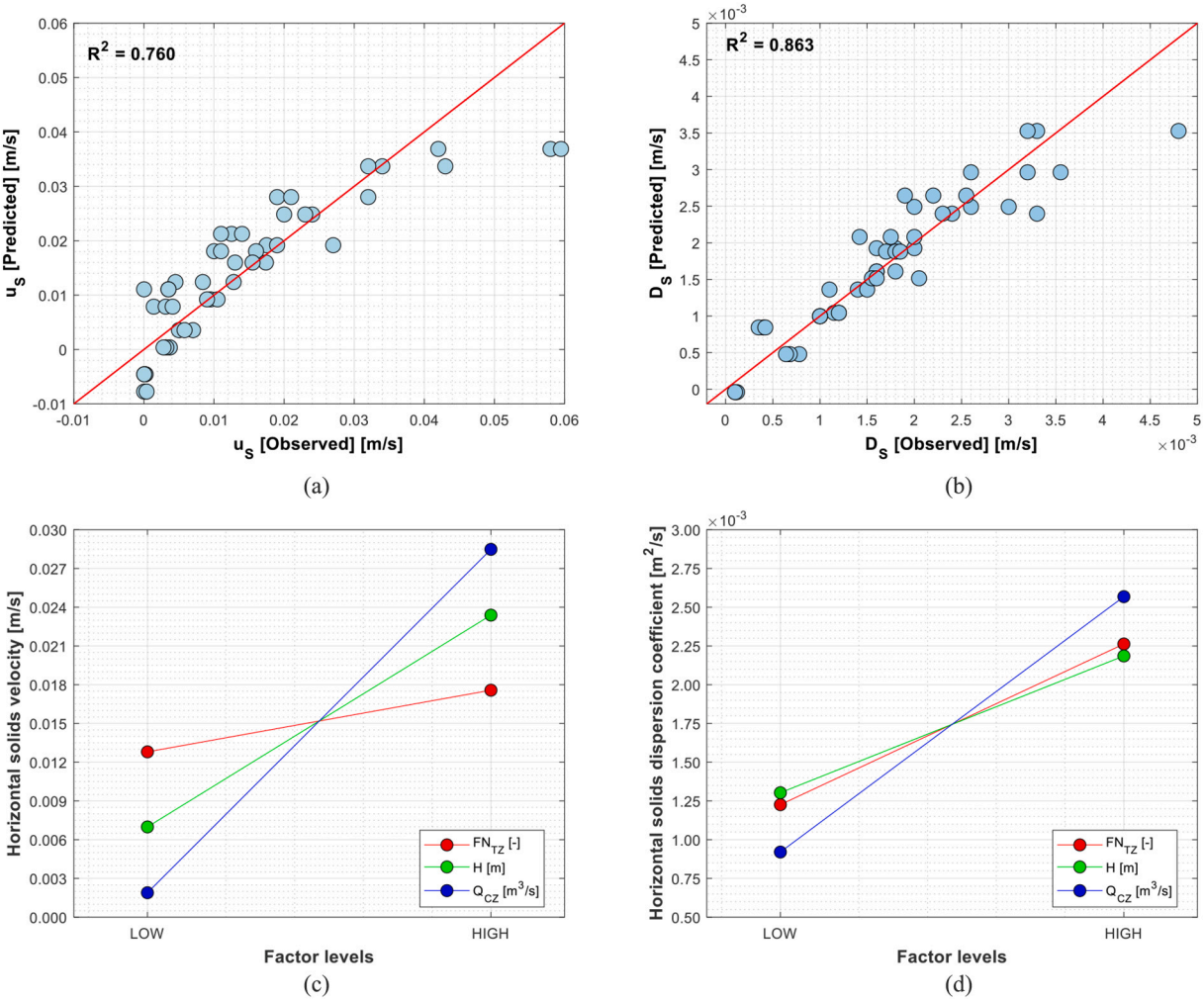

Fig. A.7. Regression model results. Predicted vs. observed plots for the horizontal (a) solids velocity, and (b) solids dispersion coefficient. Main effects plots for the horizontal (c) solids velocity, and (d) solids dispersion coefficient.

Appendix E

Fig. A.8 and Fig. A.9 provide illustrative examples of the compartment model fitting, incorporating RTD curves extracted from experimental data, after implementation of the deconvolution technique.

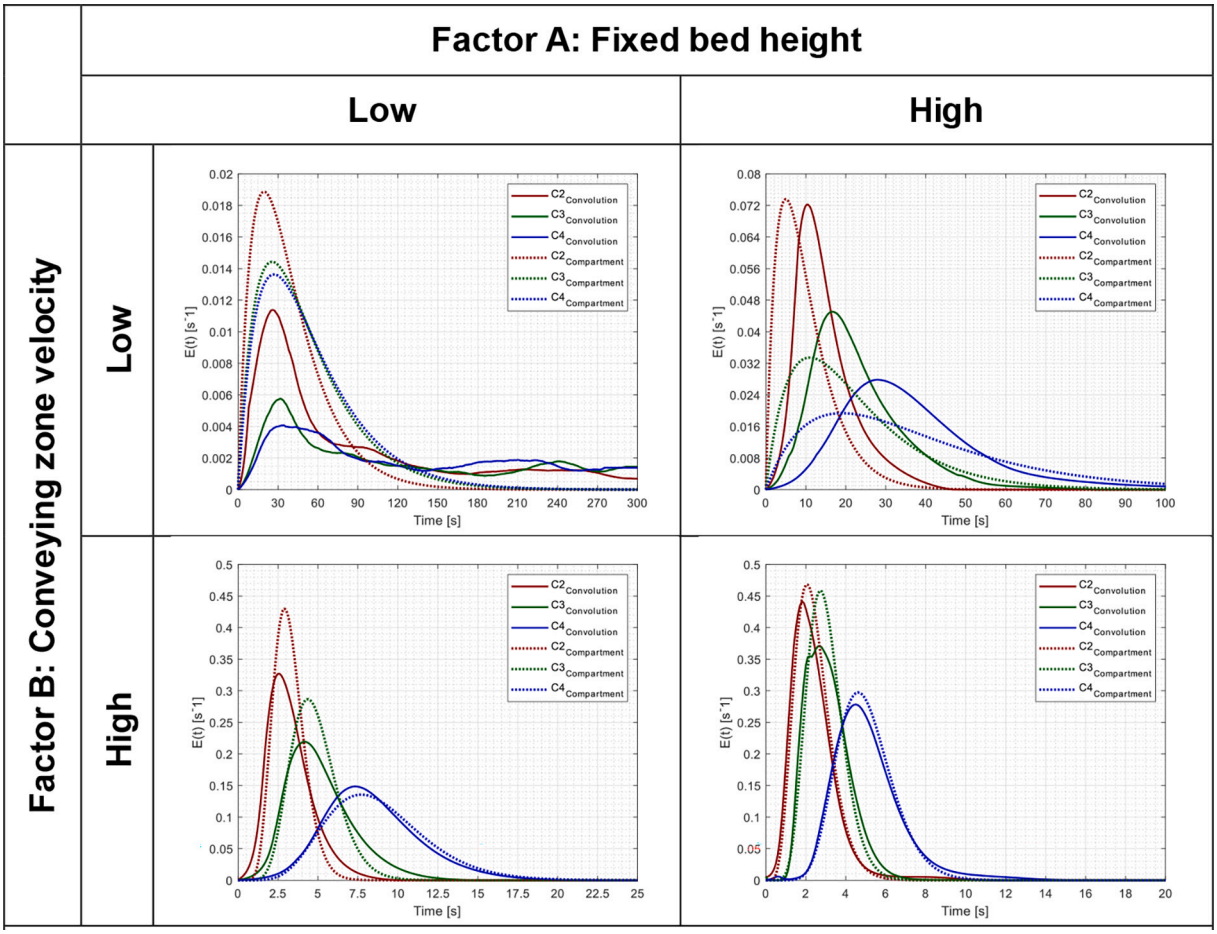

Fig. A.8. Experimental exit-age distribution profiles fitted with the compartment model for the operational condition of $FN_{TZ} = 1.83$.

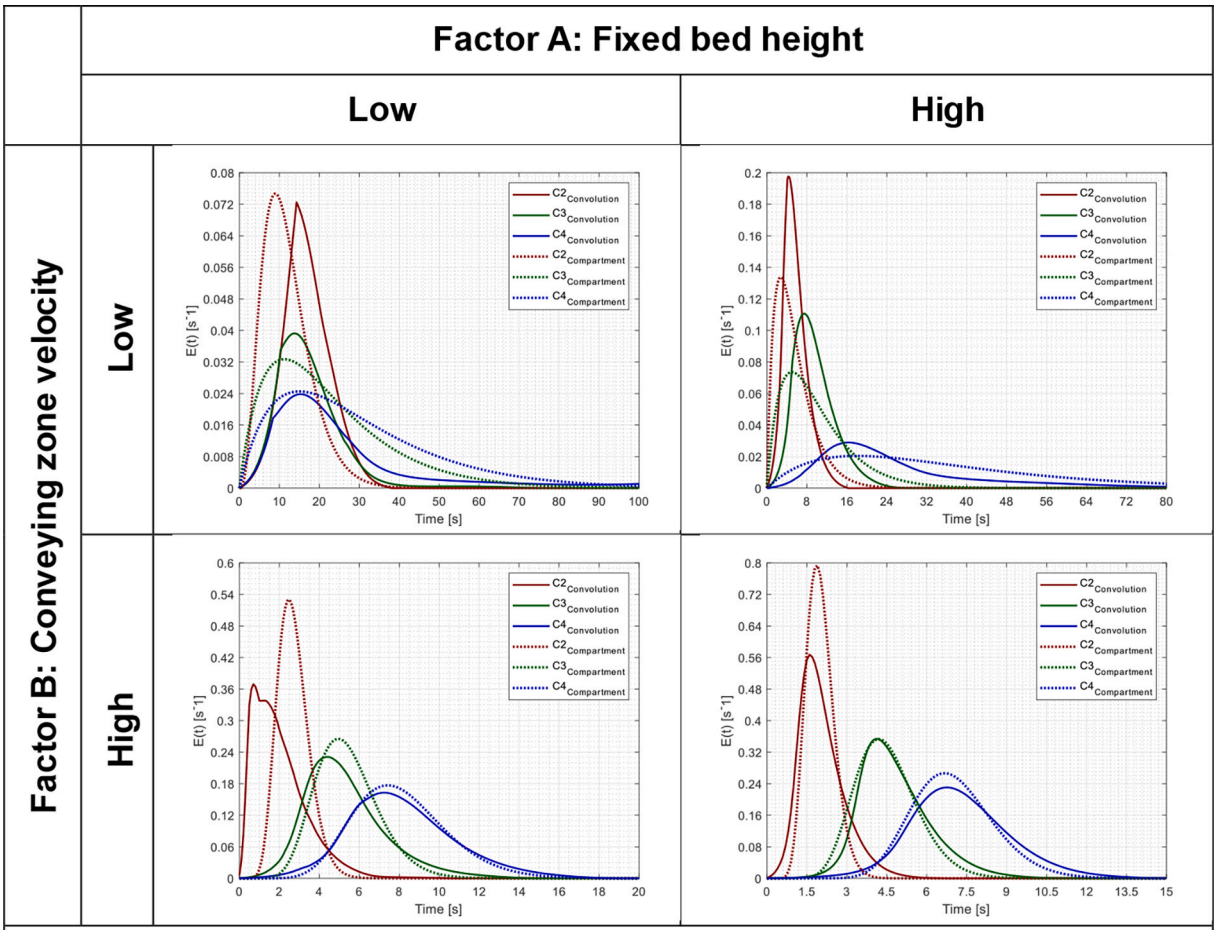

Fig. A.9. Experimental exit-age distribution profiles fitted with the compartment model for the operational condition of $FN_{TZ} = 3$.

Appendix F

Fig. A.10 illustrates the data processing steps applied to the raw concentration signals. These steps include an initial low-pass filtering to attenuate high-frequency noise (Fig. A.10**b**) and a subsequent 10th-degree polynomial fitting to further smoothen the signal while preserving its characteristic shape (Fig. A.10**c**). It is important to note the crucial role of the low-pass filtering (yielding the subtle differences between data in Fig. A.10**a** and **A.10b**) which may vary across experiments depending on the significance of experimental noise.

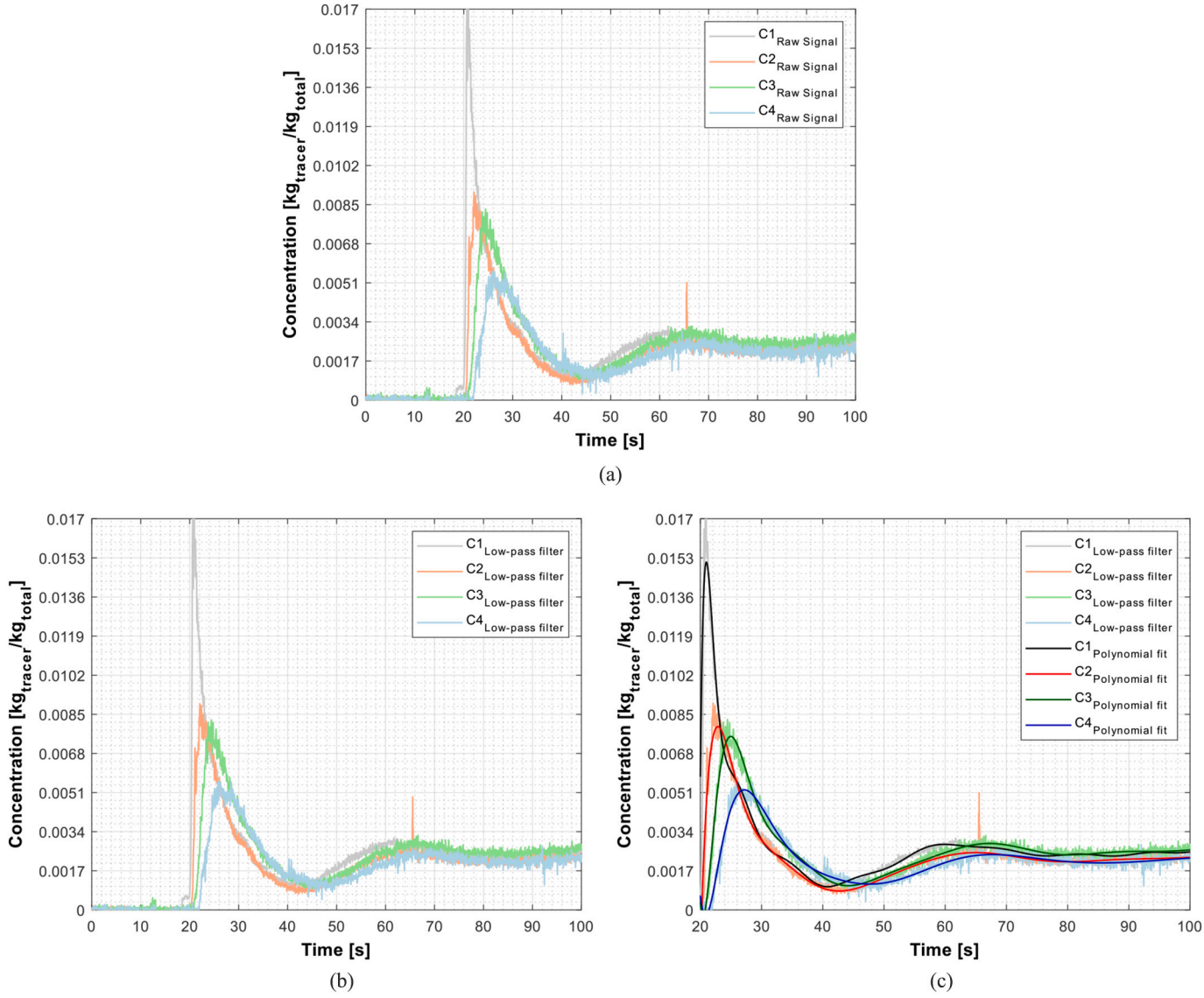

Fig. A.10. Processing of concentration signals, showcasing the initial raw data (a), low-pass filtering (b), and polynomial fitting (c). Conditions: $FN_{TZ} = 3$, H = 0.08 m, $Q_{CZ} = 0.0143\ m^3/s$.

Appendix G

Fig. 12, which shows the solids velocity versus lateral dispersion, is selected for error magnitude analysis as it presents the results in their original form. The solids velocity from the 1D convection-dispersion model can be converted into mean residence time using the characteristic length, although deriving the variance parameter is more challenging. The deconvolution technique can extract variance from the *E*-curve, as shown in Fig. A.11. Fig. A.11**a** displays the model derived from the convection-dispersion equation alongside the corresponding experimental data. Fig. A.11**b** illustrates the E-curve obtained through deconvolution based on the model acquired.

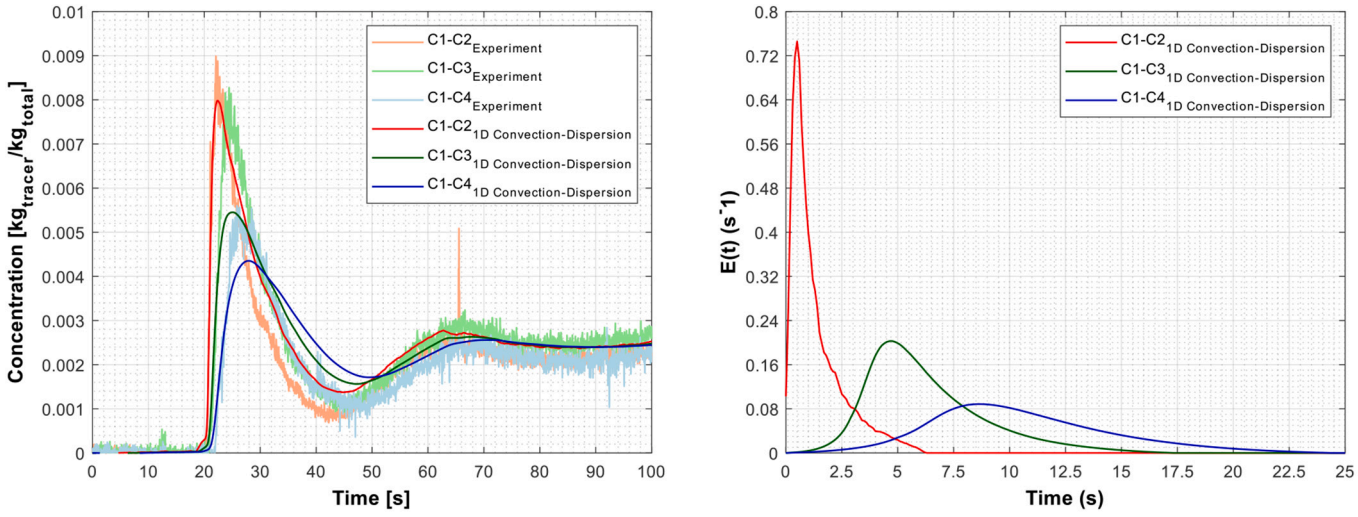

(a) Measured & modeled transient concentrations of the solids tracer.

(b) E-curves derived from modeled transient curves between Coil 1 and Coils 2-4, calculated using the deconvolution technique.

Fig. A.11. E-curve extraction, based on the 1D convection-dispersion model. Conditions: $FN_{TZ} = 3$, $H = 0.08$ m, $Q_{CZ} = 0.0143$ m^3/s.

The aforementioned approach further allows for the extraction parameters – mean residence time and variance – from the E-curve obtained after deconvolution. Fig. A.12 compares the error metrics using two different combinations. Fig. A.12**a** shows the combination used in this paper, focusing on the solids velocity-solids dispersion coefficient. Fig. A.12**b** uses the same experimental data but with a different metric combination — mean residence time and variance. However, merging these results with other methods could compromise the reliability of the comparison.

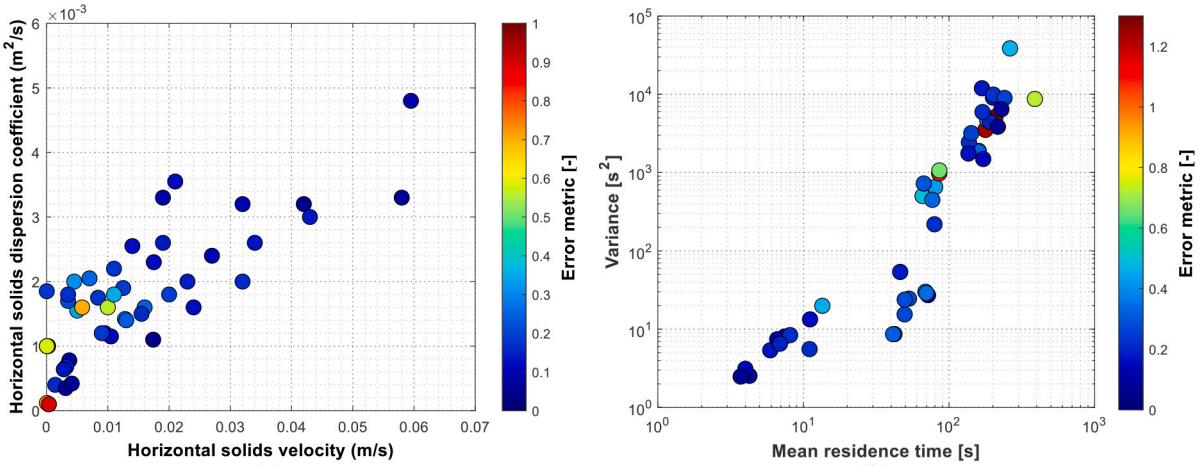

(a) (b)

Fig. A.12. Analyzing error magnitude in parameter estimations with the 1D transient convection-dispersion model.

Fig. A.13 presents a comparison of the errors obtained with the three techniques using Eq. (11) in **Section 4.4** In contrast to the error assessment plot provided in the article (Fig. 7), the variance depicted in Fig. A.13 for the 1D convection-dispersion equation undergoes a secondary processing stage that involves deconvolution. It is crucial to recognize that this additional level of processing may introduce further errors, compounding those from the initial fitting of the 1D convection-dispersion model. Therefore, to mitigate the complexities associated with multi-stage processing, the error metric focuses solely on the solids velocity parameter, as presented in Fig. 7.

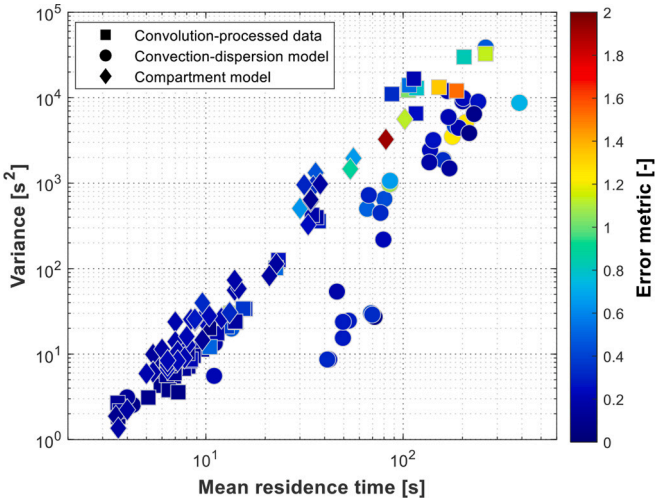

Fig. A.13. Comparison of the mean residence time and variances among the three analysis methods, together with the error metric.

Appendix H

Fig. A.14 illustrates how the Péclet number, *Pe*, depends on the solids velocity under four different operational conditions. At lower solids velocities, the *Pe* tends to increase in a roughly linear fashion with the velocity. However, at higher velocities — conditions represented only in the two data series with higher beds — the *Pe* seems to reach a plateau value. It is important to note that the high-velocity data-points, especially in the series shown in red (FN_{TZ} = 3, H = 0.1 m), are less-definitive due to significant uncertainty, unlike the clearer trend observed in the series shown in blue (FN_{TZ}= 1.83, H = 0.1 m). These data suggest that achieving a plug flow pattern in the solids crossflow by merely increasing the velocity might not be straightforward, given the enhanced back-mixing of solids linked to higher velocities.

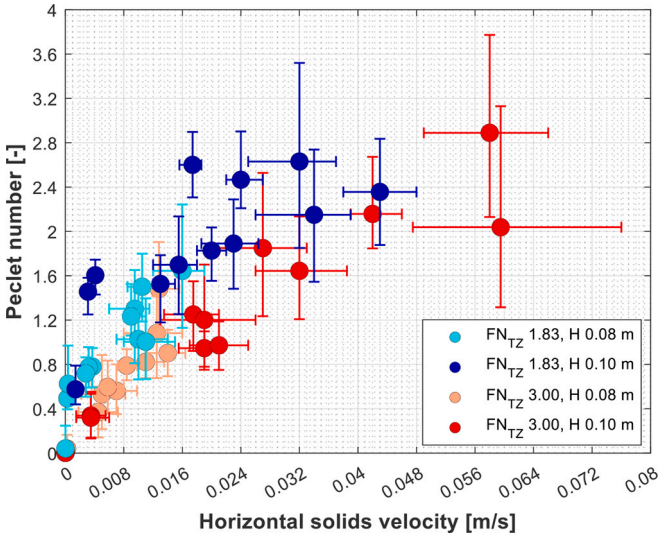

Fig. A.14. Plot of Péclet number '*Pe*' versus horizontal solids velocity 'u_S'.

References

[1] P. Basu, Combustion and Gasification in Fluidized Beds, CRC press, 2006.

[2] F. Winter, B. Schratzer, 23 - applications of fluidized bed technology in processes other than combustion and gasification, in: F. Scala (Ed.), Fluidized Bed Technologies for Near-Zero Emission Combustion and Gasification, Woodhead Publishing, 2013, pp. 1005–1033, https://doi.org/10.1533/9780857098801.5.1005.

[3] D. Kunii, O. Levenspiel, Fluidization Engineering, Butterworth-Heinemann, Boston, 1991.

[4] J.G. Yates, Fundamentals of Fluidized Bed Chemical Processes, Butterworth Publishers, Stoneham, MA, United States, 1983. https://www.osti.gov/biblio/7129060.

[5] C. Wang, J. Zhu, Circulating fluidized beds, in: Essentials of Fluidization Technology, 2020, pp. 239–268, https://doi.org/10.1002/9783527699483.ch12.

[6] D.S. Pawar, R.K. Surwase, S.B. Bhamare, S.P. Pagar, Fluidized bed granulation: a promising technique, Int. J. Pharm. Sci. Rev. Res. 64 (2020) 133–140, https://doi.org/10.47583/ijpsrr.2020.v64i02.022.

[7] L.S. Fan, Chemical Looping Systems for Fossil Energy Conversions, Wiley, 2011. https://books.google.se/books?id=WDVldP9YUPkC.

[8] W. Kong, B. Wang, J. Baeyens, S. Li, H. Ke, T. Tan, H. Zhang, Solids mixing in a shallow cross-flow bubbling fluidized bed, Chem. Eng. Sci. 187 (2018) 213–222, https://doi.org/10.1016/j.ces.2018.04.073.

[9] S. Geng, Y. Qian, J. Zhan, H. Zhang, G. Xu, X. Liu, Prediction of solids residence time distribution in cross-flow bubbling fluidized bed, Powder Technol. 320 (2017) 555–564, https://doi.org/10.1016/j.powtec.2017.07.085.

[10] E. Sette, D. Pallarès, F. Johnsson, Influence of bulk solids cross-flow on lateral mixing of fuel in dual fluidized beds, Fuel Process. Technol. 140 (2015) 245–251, https://doi.org/10.1016/j.fuproc.2015.09.017.
[11] D.C. Guío-Pérez, T. Pröll, H. Hofbauer, Solids residence time distribution in the secondary reactor of a dual circulating fluidized bed system, Chem. Eng. Sci. 104 (2013) 269–284, https://doi.org/10.1016/j.ces.2013.08.047.
[12] K. Vollmari, H. Kruggel-Emden, Numerical and experimental analysis of particle residence times in a continuously operated dual-chamber fluidized bed, Powder Technol. 338 (2018) 625–637, https://doi.org/10.1016/j.powtec.2018.07.061.
[13] L. Hua, H. Zhao, J. Li, Q. Zhu, J. Wang, Solid residence time distribution in a cross-flow dense fluidized bed with baffles, Chem. Eng. Sci. 200 (2019) 320–335, https://doi.org/10.1016/j.ces.2019.01.054.
[14] P. Schlichthaerle, J. Werther, Solids Mixing in the Bottom Zone of a Circulating Fluidized Bed. www.elsevier.comrlocaterpowtec, 2001.
[15] L. Gan, X. Lu, Q. Wang, Q. Hu, Y. Chen, J. Xu, Experimental study on lateral mixing of particles in a quasi-slot-rectangular spouted bed, Powder Technol. 243 (2013) 1–8, https://doi.org/10.1016/j.powtec.2013.03.021.
[16] O. Levenspiel, Chemical Reaction Engineering, 3rd ed, Wiley, New York, 1999.
[17] O. Levenspiel, Tracer Technology, Springer New York, 2012, https://doi.org/10.1007/978-1-4419-8074-8.
[18] J. Grace, X. Bi, N. Ellis, Essentials of Fluidization Technology, Wiley, 2020, https://doi.org/10.1002/9783527699483.
[19] A. Gómez-Barea, B. Leckner, Modeling of biomass gasification in fluidized bed, Prog. Energy Combust. Sci. 36 (2010) 444–509, https://doi.org/10.1016/j.pecs.2009.12.002.
[20] E. Sette, D. Pallarès, F. Johnsson, Experimental evaluation of lateral mixing of bulk solids in a fluid-dynamically down-scaled bubbling fluidized bed, Powder Technol. 263 (2014) 74–80, https://doi.org/10.1016/j.powtec.2014.04.091.
[21] E. Sette, T. Berdugo Vilches, D. Pallarès, F. Johnsson, Measuring fuel mixing under industrial fluidized-bed conditions – a camera-probe based fuel tracking system, Appl. Energy 163 (2016) 304–312, https://doi.org/10.1016/j.apenergy.2015.11.024.
[22] H.K. Versteeg, W. Malalasekera, An Introduction to Computational Fluid Dynamics: The Finite Volume Method, 2nd ed, Pearson Education Ltd, Harlow, England ; New York, 2007.
[23] L.R. Glicksman, Scaling relationships for fluidized beds, Chem. Eng. Sci. 39 (1984) 1373–1379, https://doi.org/10.1016/0009-2509(84)80070-6.
[24] L.R. Glicksman, M. Hyre, K. Woloshun, Simplified Scaling Relationships for Fluidized Beds, 1993.
[25] D.C. Guío-Pérez, T. Pröll, H. Hofbauer, Measurement of ferromagnetic particle concentration for characterization of fluidized bed fluid-dynamics, Powder Technol. 239 (2013) 147–154, https://doi.org/10.1016/j.powtec.2013.01.040.
[26] M. Farha, D.C. Guío-Pérez, J. Aronsson, F. Johnsson, D. Pallarès, Assessment of experimental methods for measurements of the horizontal flow of fluidized solids under bubbling conditions, Fuel 348 (2023) 128515, https://doi.org/10.1016/j.fuel.2023.128515.
[27] A.S. Morris, R. Langari, Chapter 3 - measurement uncertainty, in: A.S. Morris, R. Langari (Eds.), Measurement and Instrumentation, Butterworth-Heinemann, Boston, 2012, pp. 39–102, https://doi.org/10.1016/B978-0-12-381960-4.00003-6.
[28] R. Martin, Noise power spectral density estimation based on optimal smoothing and minimum statistics, IEEE Trans. Speech Audio Proc. 9 (2001) 504–512, https://doi.org/10.1109/89.928915.
[29] L. Zhongshen, Design and ANALYSIS OF IMPROVED butterworth low pass filter, in: 2007 8th International Conference on Electronic Measurement and Instruments, 2007, https://doi.org/10.1109/ICEMI.2007.4350554, pp. 1-729-1–732.
[30] E. Carbonneau, R. Fontaine, C. Smeesters, A Practical Approach to Determine Appropriate Cutoff Frequencies for Motion Analysis Data, 2013.
[31] W.H. Richardson, Bayesian-based iterative method of image restoration*, J. Opt. Soc. Am. 62 (1972) 55–59, https://doi.org/10.1364/JOSA.62.000055.
[32] D.S.C. Biggs, M. Andrews, Acceleration of iterative image restoration algorithms, Appl. Opt. 36 (1997) 1766–1775, https://doi.org/10.1364/AO.36.001766.
[33] R. Martí, Multi-start methods, in: F. Glover, G.A. Kochenberger (Eds.), Handbook of Metaheuristics, Springer US, Boston, MA, 2003, pp. 355–368, https://doi.org/10.1007/0-306-48056-5_12.
[34] E. Sette, D. Pallarès, F. Johnsson, Experimental evaluation of lateral mixing of bulk solids in a fluid-dynamically down-scaled bubbling fluidized bed, Powder Technol. 263 (2014) 74–80, https://doi.org/10.1016/j.powtec.2014.04.091.